Developmental emergence of two-stage nonlinear synaptic integration in cerebellar interneurons

Abbreviated title: **Development of neuronal computation in interneurons**

Célia Biane [1], Florian Rückerl [3], Therese Abrahamsson [3],Cécile Saint-Cloment [3], Jean Mariani [1], Ryuichi Shigemoto [4], David A. DiGregorio [3] Rachel M. Sherrard [1] and Laurence Cathala [1,2*]

[1] Sorbonne Université et CNRS UMR 8256, Adaptation Biologique et Vieillissement 9 Quai St Bernard, 75005 Paris, France

[2] Paris Brain Institute, CNRS UMR 7225 - Inserm U1127 – Sorbonne UniversitéGroupe Hospitalier Pitié Salpêtrière 47 Boulevard de l'Hôpital 75013 Paris France

[3] Department of Neuroscience, Institut Pasteur, 25 rue du Dr Roux, 75724 Paris Cedex 15, France; CNRS URA 21821

[4] Institute of Science and Technology Austria, Am Campus 1, 3400 Klosterneuburg, Austria

*Corresponding author: Laurence Cathala (Laurence.cathala@sorbonne-universite.fr)

Celia Biane : celiabiane1@gmail.com

Florian Rückerl : florian.ruckerl@pasteur.fr

Therese Abrahamsson: therese.abrahamsson@gmail.com

Cécile Saint-Cloment : cecile.saint-cloment@pasteur.fr

David DiGregorio : david.digregorio@pasteur.fr

Ryuichi Shigemoto: ryuichi.shigemoto@ist.ac.at

Rachel Sherrard : rachel.sherrard@sorbonne-universite.fr

Jean Mariani : jean.mariani@sorbonne-universite.fr

Abstract

Synaptic transmission, connectivity, and dendritic morphology mature in parallel during brain development and are often disrupted in neurodevelopmental disorders. Yet how these changes influence the neuronal computations necessary for normal brain function are not well understood. To identify cellular mechanisms underlying the maturation of synaptic integration in interneurons, we combined patch-clamp recordings of excitatory inputs in cerebellar stellate cells (SCs), 3D-reconstruction of SC morphology with excitatory synapse location, and biophysical modeling. We found that, during development, synaptic strength was homogeneously reduced along the somato-dendritic axis, but that dendritic integration was always sublinear. However, dendritic branching increased without changes in synapse density, leading to a substantial gain in distal inputs. Thus, changes in synapse distribution, rather than dendrite cable properties, are the dominant mechanism underlying the maturation of neuronal computation. These mechanisms favor the emergence of a spatially compartmentalized two-stage integration model promoting location-dependent integration within dendritic subunits.

Introduction

Dendritic integration of spatio-temporal synaptic activity is fundamental to neuronal computation, which shapes the transformation of input activity into output spiking (Silver, 2010). In particular, the cable properties of dendritic trees generate isolated electrical compartments that produce non-linear integration of synaptic potentials. These compartments increase the computational power of single neurons (Caze et al., 2013; Poirazi and Mel, 2001) and are a prominent feature of human neurons (Beaulieu-Laroche et al., 2018; Gidon et al., 2020). Dendritic morphology and ion channel expression are developmentally regulated, but how they contribute to the maturation of neuronal computations throughout post-natal circuit formation and refinement is less well known. The observation of alterations in dendritic morphology, synaptic connectivity, density, and function in several neurodevelopmental disorders (Marín, 2016; Penzes et al., 2011) indicates that both appropriate neuronal wiring *and* the maturation of a neuron's integrative properties are necessary to develop fully functional neuronal networks (Pelkey et al., 2015).

The type and number of computations that a neuron can perform depend on the diversity of the mathematical operations used to combine synaptic inputs within dendritic trees. These can be sublinear, linear, or supralinear (Branco and Häusser, 2011; Caze et al., 2013; Poirazi and Mel, 2001; Tran-Van-Minh et al., 2015; Vervaeke et al., 2012). Nonlinear dendritic operations depend on (1) dendritic architecture and associated membrane properties (Abrahamsson et al., 2012; Hu et al., 2010; Katz et al., 2009; Larkum et al., 2009; Magee, 1999, 2000; Nevian et al., 2007; Rall, 1967), (2) spatial localization, density, and properties of synapses across the dendritic arbor (Grillo et al., 2018; Larkum et al., 2009; Losonczy et al., 2008; Losonczy and Magee, 2006; Menon et al., 2013; Schiller et al., 2000; Williams and Stuart, 2002) and (3) the spatiotemporal synaptic activity pattern (Bloss et al., 2018; Grillo et al., 2018; McBride et al., 2008; Scholl et al., 2017; Xu et al., 2012). All these factors change during neuronal circuit maturation through cell-autonomous or activity-dependent processes (Sigler et al., 2017) (Katz and Shatz, 1996). Indeed the maturation of neuronal excitability and morphology (Cathala et al., 2003; Cline, 2016; McCormick and Prince, 1987; Zhang, 2004) is associated with restriction of neuronal connectivity to subcellular compartments (Ango et al., 2004), activity-dependent synaptic rearrangement (Chen and Regehr, 2000; Cline, 2016; Kwon and Sabatini, 2011; Li et al., 2011) and the maturation of excitatory (Cathala et al., 2003; Hestrin, 1992; Koike-Tani et al., 2005; Lawrence and Trussell, 2000; Taschenberger and von Gersdorff, 2000) and inhibitory synaptic inputs (Ben-Ari, 2002; Sanes, 1993; Tia et al., 1996). Despite this knowledge, how developmental changes in cellular parameters dictate dendritic operations and their associated neuronal computations, remains largely unexplored.

Interneurons are fundamental to normal circuit function throughout development. They contribute to the developmental regulation of critical periods (Hensch et al., 1998; Gu et al., 2017), are important for establishing direction selectivity in the retina (Wei et al., 2011), and their dysfunction is associated with neurodevelopment disorders (Akerman and Cline, 2007; Le Magueresse, 2013; Marin, 2016). Parvalbumin-positive (PV+) GABAergic interneurons are found in the neocortex, hippocampus, and cerebellum, and all share anatomical and functional features (Hu et al., 2014). These inhibitory interneurons provide precise temporal control of the excitatory drive onto principal neurons (Mittmann et al., 2005; Pouille and Scanziani, 2001). Cerebellar stellate cells (SCs) are PV+ and receive excitatory inputs from granule cells, and in turn modulate the excitability and firing precision of the cerebellar output neurons, Purkinje cells (Arlt and Häusser, 2020; Häusser and Clark, 1997; Mittmann et al., 2005). The thin SC dendrites (~0.4 μm diameter) filter synaptic potentials as they propagate to the soma and confer sublinear summation of synaptic input (Abrahamsson et al., 2012; Tran-Van-Minh et al., 2015). Nevertheless, the mechanisms underlying the maturation of these dendritic operations and neuronal computation of interneurons has not been explored.

Here we study in detail the maturation of the synaptic and integrative properties of SCs in the cerebellar cortex. We combined patch-clamp recording with fluorescence-guided electrical stimulation, fluorescence and electron microscopy 3D reconstructions, and numerical simulations, to examine synapse strength and spatial distribution. Unlike unitary inputs in other neuron types, we found that adult SCs had smaller and slower miniature excitatory postsynaptic currents (mEPSCs) than those observed in immature SCs. This could be explained by enhanced electrotonic filtering since immature SCs are thought to be electrotonically compact (Carter and Regehr, 2002; Llano and Gerschenfeld, 1993). We found, however, that their dendrites are as thin as in adult SCs and also capable of robust electrotonic filtering and sublinear summation of synaptic inputs. Using a novel fluorescence synaptic tagging approach we found a significantly larger contribution of distal dendritic synapses in adult SCs, due to a substantial increase in dendritic branching combined with constant synapse density. Multicompartment biophysical modeling confirmed that developmental changes in synapse distribution could reproduce the developmental reduction and slowing of recorded mEPSCs as well as the increased sublinear integration observed in adult SCs. Our findings provide evidence that SCs implement different neuronal computations throughout development: A predominant global summation model in immature SCs shifts to sublinear dendritic integration in adult SCs, favoring the developmental emergence of the two-layer integration model. This work provides a mechanistic description of the maturation of neuronal computation resulting from both functional and anatomical

changes in synaptic transmission and integration. Our findings and approach also provide a framework for interpreting the functional implications of alterations in dendritic morphology and connectivity on information processing within neural circuits during disease.

Results

AMPAR-mediated mEPSCs become smaller and slower during development

The strength and time course of synaptic transmission is fundamental to information processing within neural networks since they influence the efficacy and temporal precision of the transformation of synaptic inputs into neuronal outputs. Excitatory synaptic inputs trigger postsynaptic conductance changes due to the opening of neurotransmitter-gated receptors which are activated upon transmitter release. These conductance changes are locally integrated within dendrites into excitatory postsynaptic potentials (EPSPs), which then propagate to the soma where they contribute to somatic voltage. The strength and time course of synaptic conductances are known to change during development (Cathala et al., 2003; Chen and Regehr, 2000; Koike-Tani et al., 2005) and can affect dendritic integration, which in turn may alter neuronal computation (Tran-Van-Minh et al., 2015).

To identify factors that shape the post-natal developement of SC integrative properties, we first compared excitatory postsynaptic currents (EPSCs) recorded in acute brain slices, either from immature SCs soon after they reach their final position in the outer layer of the cerebellar cortex (postnatal days 13 to 17), or from adult SCs (post-natal ages 35 to 57). Granule cell afferent (parallel fibers, PFs) synapses release glutamate from only one synaptic vesicle, despite the presence of multiple release sites per synaptic contact (Foster et al., 2005). We, therefore, examined these physiologically relevant "quantal synaptic events" using somatic recordings of spontaneously occurring AMPA receptor (AMPAR)-mediated miniature EPSCs (mEPSCs) in the presence of TTX to block spontaneous presynaptic activity. mEPSCs arise from the release of a single neurotransmitter vesicle and occur randomly at all synapses converging onto a single neuron. Therefore, mEPSCs can provide an unbiased assessment of the effective distribution of synaptic strengths throughout the entire somato-dendritic compartment.

We found that AMPAR-mediated mEPSCs occurred with a similar frequency at both ages (1.37 ± 0.27 *vs.* 1.14 ± 0.13 Hz, $P>0.05$), but mEPSCs were significantly smaller and slower in the adult (Figures 1A-1C). In immature SCs the average mEPSC amplitude was 48 ± 7 pA, with 10-90% rise and decay times (τ_{decay}, see Methods) of 0.16 ± 0.01 ms and 0.68 ± 0.06 ms respectively. In contrast, mEPSCs from adult SCs were smaller 24 ± 2 pA ($P<0.05$), with slower rising (0.24 ± 0.02 ms; $P<0.05$) and decaying kinetics (τ_{decay} = 1.31 ± 0.14 ms; $P<0.05$). The mEPSC amplitudes are consistent with those from previous studies describing large miniature events (Llano and Gerschenfeld, 1993) capable of influencing immature SC firing (Carter and Regehr, 2002). Nevertheless, we observed that mEPSCs continue to mature past the 3rd post-natal week, becoming smaller and slower.

Previous studies have described developmental alterations in the glutamate content of synaptic vesicles (Yamashita, 2003) and synaptic structure (Cathala et al., 2005), both of which can modulate the neurotransmitter concentration in the synaptic cleft. To test whether the reduced amplitude and slower time-course could be due to alteration in *effective* amplitude and time-course of glutamate concentration ([Glut]) seen by synaptic AMPARs, we recorded mEPSCs in the presence of a rapidly dissociating, low-affinity competitive AMPAR antagonist, γDGG (Diamond and Jahr, 1997; Liu et al., 1999). Application of a submaximal concentration of γDGG (1 mM) reduced mEPSC peak amplitude (Figure 1D, paired $P<0.05$) similarly at both ages (44.42 ± 4.36 %, n = 7 in the immature *vs.* 42.38 ± 3.69 %, n = 9 in the adult, $P>0.05$; Figure 1E), with no apparent effect on mEPSC kinetics (Figure 1F, paired $P>0.05$). This result suggests that the decreased amplitude and slowing of mEPSCs is unlikely due to a change in the synaptic [Glut]. We, therefore, explored whether post-synaptic mechanisms, such as the acquisition of dendritic electrotonic filtering, (which exists in adult SCs (Abrahamsson et al., 2012) and/or lower synaptic conductance (i.e., the number of activated synaptic AMPARs), could explain the changes in mEPSC during maturation.

Dendritic morphology supports electrotonic filtering in both immature and adult SCs

Dendrites of adult SCs exhibit electrotonic cable filtering, which reduces the amplitude of synaptic responses and slows their time course as they propagate to the soma (Abrahamsson et al., 2012), thus modifying mEPSCs recorded at the soma. We considered whether the developmental difference in mEPSC amplitude and kinetics was due to the development of electrotonic filtering. To test this hypothesis, we estimated the dendrite diameter of immature SCs, because the small diameter (<0.5 µm) and rapid synaptic conductances of adult SC dendrites underlie their cable filtering properties (Abrahamsson et al., 2012). The dendritic diameter was estimated from the full-width at half-maximum (FWHM) of the fluorescence profile perpendicular to the dendrite from confocal images of live SCs aged P13 to P17 filled with Alexa 488 (Figure 2A). Diameters ranged from 0.26 µm to 0.93 µm with a mean of 0.47 ± 0.01 µm (n = 93 dendritic segments of 18 neurons; Figure 2B), which is close to the average adult value of 0.41 ± 0.02 µm (range 0.24 to 0.9 µm, n = 78 dendrites; data from Abrahamsson et al., 2012; $P<0.05$).

To understand the potential functional influence of such small diameters, we calculated the dendritic space constant (see Methods), i.e. the distance along a cable over which a steady-state membrane voltage decreases by 1/*e*. Using the estimated 0.47 µm dendritic diameter, membrane resistance (R_m) of 20,000 Ohm.cm^2 (matching that experimentally measured from immature SCs membrane time constant τ_m of 19 ± 2.2 ms, n = 16) and an internal resistivity R_i ranging from 100 to 200 Ohm.cm, we calculated the steady-state dendritic space constant

(λ) to be between 343 to 485 µm, which is 3-5 fold longer than the actual dendritic length. This confirms that, for steady-state membrane voltages, immature SCs are indeed electrically compact, as previously suggested (Carter and Regehr, 2002). However, the frequency-dependent space constant (λ_f; assuming that rapid mEPSCs are well-approximated by a 1 kHz sine wave), was calculated to be between 46 to 60 µm (for R_i of 100 - 200 Ohm·cm). These values are less than dendrite lengths and suggest that, like in adult SCs (Abrahamsson et al., 2012), somatic recording of EPSC originating in dendrites may be smaller and slowed due to electrotonic cable filtering.

We confirmed these frequency-dependent estimations using a multi-compartmental biophysical model to simulate the somatic response to quantal synaptic release throughout the somato-dendritic compartment. We first used an idealized SC dendritic morphology (Abrahamsson et al., 2012) and then fully reconstructed immature SC dendritic trees. For the idealized immature SC morphology (Figure 2C), we used an 8 µm soma diameter (8.07 ± 0.23 µm, estimated from confocal images of 31 immature SC somata) and a 0.47µm dendritic diameter (see mean value from Figure 2B), an R_m of 20,000 Ohm.cm^2 and an R_i of 100 - 200 Ohm·cm. The simulated synaptic conductance g_{syn} amplitude and time course were adjusted to match quantal EPSCs generated by a single vesicle (qEPSC; see experimental approach below and Figure 3) recorded following activation of somatic synapses. Simulated qEPSCs were large and fast for synapses located at the soma (magenta trace, Figure 2C) and 72% smaller and 200% slower when synapses were located on the dendrites (grey trace; for a synapse at 47 µm on a dendrite with 3 branch points and an intermediate R_i of 150 Ohm·cm). This decrease in amplitude was associated with a large increase in the local synaptic depolarization (green trace, Figure 2C) that would substantially reduce the local driving force during synaptic transmission onto dendrites, causing a sublinear read-out of the underlying conductance, similar to that observed in adult SCs (Abrahamsson et al., 2012).

We obtained similar results with morphologically accurate passive biophysical models derived from 3D reconstructed SCs. SCs were patch-loaded with the fluorescence indicator Alexa 594, imaged with two-photon laser scanning microscopy (2PLSM; Figure 2D), and then reconstructed with *NeuronStudio* (Rodriguez et al., 2008). The 3D reconstruction was then imported into the simulation environment, *Neuron,* with the membrane properties indicated above. Activation of a synaptic contact at 60 µm from the soma on any dendrite of the reconstructed immature P16 SC, produced a simulated qEPSC that was consistently smaller and slower (grey traces) than the one produced following the activation of a somatic synapse (magenta trace; Figure 2E). Similarly, activation of synaptic inputs along a dendrite, at increasing distance from the soma, produced soma-recorded qEPSCs that become smaller and slower with distance (Figure 2F), similar to those in reconstructed adult SCs (Figure 2G,

2H) and idealized SC models (Abrahamsson et al., 2012). These simulations suggest that, like their adult counterparts, the morphometric characteristics of immature SCs should also produce significant cable filtering of both the amplitude and time course of EPSCs.

Synaptic events are electrotonically filtered in immature SCs

To confirm modeling predictions, we next explored whether dendrite-evoked quantal events in immature SCs show evidence of cable filtering. Taking advantage of the orthogonal projection of parallel fibers (PFs), we used parasagittal cerebellar slices to stimulate specific PF beams that are synaptically connected to well-defined regions of an Alexa 594 loaded SC by placing an extracellular electrode either above the soma or close to the distal part of an isolated dendrite branch (Figure 3A and 3B). We recorded evoked qEPSCs using whole-cell voltage clamp of the SC soma. This approach allows precise control of the location of the activated synapses, in contrast with mEPSCs that can arise from unknown synapse locations anywhere along the somato-dendritic axes. Dendritic filtering could then be examined by measuring the amplitude and time course (response width at half-peak, half-width) of these synaptic events, typically used to estimate cable filtering (Rall, 1967). To isolate qEPSCs, PFs were stimulated in low release probability conditions (EPSC success rate of less than 10%; 0.5 mM extracellular [Ca^{2+}] and 5 mM [Mg^{2+}]). In these conditions, the average EPSC generated from all successful trials is a good approximation of the quantal current amplitude and time course (Silver et al., 2003). When stimulating somatic synapses, qEPSCs recorded at the soma had a mean peak amplitude of 62 ± 3 pA, a 10-90 % rise time of 0.14 ± 0.004 ms, and a half-width of 0.60 ± 0.02 ms (n = 25; Figure 3C, 3D). In contrast, stimulation of dendritic synapses produced somatically recorded qEPSCs that were significantly smaller (mean amplitude: 46 ± 3 pA) and slower (10-90 % rise time of 0.24 ± 0.012 ms and a half-width of 0.88 ± 0.04 ms; n = 18; all $P<0.05$, Figure 3C, 3D). These results are consistent with cable filtering of EPSCs as they propagate along dendrites in immature SCs.

The decreased amplitude of qEPSCs evoked in the dendrite could also be due to lower AMPAR content of dendritic synapses. As AMPAR density in SC synapses is constant (Masugi-Tokita et al., 2007) we used post-synaptic density (PSD) size as a proxy for the number of AMPARs. We measured PSD area of somatic and dendritic synapses from 3D electron microscopy (EM) reconstruction of immature SCs. We reconstructed the soma and the dendritic tree of two SCs (P14 and P17) loaded with Alexa 594 and biocytin (Figure 3E). Immunogold labeling of biocytin made possible the identification of PSDs (Figure 3F) and measurement of their distance from the soma. PSD area was constant along somatodendritic axes (Figure 3G) ruling out synaptic scaling as a mechanism for the reduction in qEPSCs after dendritic stimulation. Thus the difference in qEPSC amplitude and time-course observed between somatic and dendritic synapses in immature SCs is likely due to cable filtering.

Developmental changes in synaptic conductance amplitude, but not time course

Because cable filtering of synaptic responses is present in both immature and adult SCs, we next explored whether differences in mEPSC amplitude between the two ages were due to maturation of quantal synaptic conductance (i.e. number of synaptic AMPARs). To avoid the effects of cable filtering, we measured qEPSCs only at somatic synapses. In immature SCs, somatic qEPSCs were 41% larger than those in adult SCs (62.3 ± 3.3 pA, n = 25 *vs.* 44 ± 2.4 pA, n = 12, Abrahamsson et al., 2012), $p<0.05$, Figure 4A, 4B), but with no difference in the half-width (0.60 ± 0.02 ms, n = 25 *vs.* 0.59 ± 0.06 ms, n = 12, $P>0.05$, Figure 4B). These results suggest that more AMPARs are activated by quantal release of glutamate at immature somatic synapses. Similarly, the 10-90 % rise time was slower in immature SCs compared to adult (0.14 ± 0.02 ms, n = 25 *vs.* 0.12 ± 0.004, n = 12, $P<0.05$; Figure 4B), indicating larger immature synapses (Cathala et al., 2005). To confirm the reduction in synaptic AMPARs during maturation, we compared somatic PSD areas between immature and adult SCs. In immature SCs, mean somatic PSD size was 0.039 ± 0.002 μm^2 (n = 83 synapses; Figure 4C), which is 39% larger than that of adult SCs (0.028 ± 0.0015 μm^2, n = 97, $P<0.05$; data obtained by the same method from Abrahamsson et al., 2012). The developmental reduction in PSD size is similar to the amplitude reduction of recorded somatic qEPSC, and thus will contribute to the developmental reduction in mEPSC. However, fewer synaptic AMPARs cannot explain the observed change in mEPSC time course.

Dendritic distribution of excitatory synaptic inputs changes during maturation

In addition to cable filtering of synaptic currents, a neuron's somatic response to dendritic input is also affected by synapse distribution within its dendritic tree, which may not be uniform – as demonstrated for starburst amacrine interneurons (Vlasits et al., 2016) and CA1 pyramidal neurons (Katz et al., 2009; Magee and Cook, 2000). We hypothesized that changes in synapse distribution could underlie the slowing of mean mEPSCs time-course observed adult SCs. In support of this hypothesis, immature SC mEPSC rise and decay kinetics are similar to those of somatic qEPSCs (compare Figure 1 *vs.* Figure 4), whereas adult SC mEPSC kinetics are closer to those of dendritic qEPSCs (Figure 1 *vs.* Figure 3). Specifically, in immature SC the mean mEPSC decay is similar to the qEPSC decay from somatic synapses but significantly different from those of dendritic synapses, suggesting that synaptic responses from distal synapses do not participate significantly to the mean mEPSC at this developmental stage. In contrast, the adult mEPSC decay is close to the dendritic qEPSC decay, but significantly different from that of somatic synapses. These results are consistent with mEPSCs in adult SCs arising more often from more distal synapses.

To test this hypothesis, we examined the distribution of excitatory synaptic inputs along the somato-dendritic compartment in immature and adult SCs. Since SC dendrites lack spines,

we used transgenic mice conditionally expressing Venus-tagged PSD95 to label putative excitatory synapses. We then mapped Venus-tagged PSD95 puncta associated with the somata and dendritic trees of Alexa 594-filled immature and adult SCs (Figure 5A-D), defining puncta located within 200 nm of the dendritic surface (Figure 5E) as excitatory synapses targeting the dendrite (Figure 5F; see Methods). Venus-tagged PSD95 puncta within the soma and dendritic tree of 9 immature and 8 adult 3D-reconstructed SCs (Figure 5G), showed ~ 80 % more puncta on adult SCs (582 ± 48 puncta *vs.* 324 ± 21 in immature SC, $p<0.05$). Synapse distribution was assessed by counting the number of PSD95 puncta within 10 µm segments at increasing distance from the soma. In immature SCs, ~ 80 % are within 35 µm of the soma, in contrast to only ~ 40% this close to the soma in adult SCs (Figure 6A, 6B). However, the ratio of detected puncta (Figure 6B) to dendritic segments (Figure 6C) shows that puncta density remained constant across the dendritic tree at both ages (Figure 6D). Thus, the larger number of puncta located further from the soma in adult SCs is not due to increased puncta density with distance, but a bigger dendritic field (Figure 6E) and many more distal dendritic branches (Sholl analysis, Figure 6F). Taken together, these data demonstrate that increased dendritic complexity during SC maturation is responsible for a prominent shift toward distal synapses in adult SCs. Therefore, if mEPSCs are generated from a homogeneous probability of release across all synapses, then this bias towards distal synapses in adult SC will generate quantal responses that experience stronger cable filtering.

Change in synapse distribution underlies developmental slowing of mEPSC

We next examined whether differences in synapse distribution could account quantitatively for the observed changes in mEPSC amplitude and time course. We performed numerical simulations using reconstructed immature and adult SCs (Figure 2D and 2G) and a quantal synaptic conductance (g_{syn}) that reproduced measured immature and adult qEPSCs induced at somatic synapses (Figure 4). We simulated qEPSCs evoked by synaptic activation at the soma and at 10 µm intervals along the somato-dendritic axes (Figure 7A). Assuming that mEPSCs are generated randomly with an equal probability at all synapses, we generated a simulated *mean mEPSC* by summing the qEPSC at each distance ($EPSC_d$), each weighted by its relative frequency according to the synapse distribution (Figure 7B). $EPSC_d$s arising from distal locations in the adult were larger and contributed relatively more to the simulated *mean* mEPSC waveform (Figure 7B). The resulting *mean mEPSC* was smaller in adult SCs than in immature SCs (26.0 ± 0.6 pA, n = 9 dendrites *vs.* 52.2 ± 0.4 pA, n = 7 for R_i 150) and its time-course had slower rise (10-90 % rise time = 0.24 ± 0.05 *vs.* 0.17 ± 0.01 ms) and decay (half-width = 1.11 ± 0.04 *vs.* 0.77 ± 0.01 ms; for all $P<0.05$). Moreover, the simulated *mean mEPSCs* lay within one standard deviation of measured experimental mEPSC values (Figure 7C, 7D). Thus by implementing the experimentally observed synapse distributions in our simulations, we could accurately reproduce the experimental mean mEPSCs. These results

demonstrate that developmental increases in dendritic branching complexity, provided that synapse density is homogeneous, can account for the changes in mEPSC kinetics (Figure 1).

Influence of synapse distribution on dendritic integration of multiple synaptic inputs

We previously showed in adult SCs that the activation of dendritic synapses conveys sublinear integration as compared to the soma (Abrahamsson et al., 2012) due to the large local input resistance of thin dendrites resulting in synaptic depolarizations that reduced synaptic current driving force (Bloomfield et al., 1987; Rall, 1967). This also produced a distance-dependent decrease in short-term plasticity (STP). We examined whether dendritic integration in immature SCs is also sublinear by comparing STP following dendritic and somatic synapse activation. PFs targeting SC somata and dendrites were stimulated using a pair of extracellular voltage pulses with an interval of 20 ms. The paired-pulse ratio (PPR; the ratio of the amplitudes of the second *vs.* the first EPSC) was 2.1 ± 0.1 for somatic synapses (n = 10) and decreased to 1.8 ± 0.1 for distal dendritic synapses (n = 15; $P<0.05$; Figure 8A), consistent with sublinear integration. These results were reproduced by numerical simulations of evoked EPSCs or EPSPs in the idealized passive SC model (with a synaptic g_{syn} matching the recorded EPSC evoked at the soma and a 2.25 conductance ratio). These findings show that immature SC dendrites also display an STP gradient, suggesting that they are capable of sublinear integration.

To address this possibility, we used biophysical modeling of subthreshold synaptic input-output relationships (I/O) that has been shown to accurately reproduce experimental sublinear I/Os recorded after neurotransmitter photo-uncaging (Abrahamsson et al., 2012). Evoked EPSPs were simulated (sim eEPSP) in response to increasing synaptic conductance (g_{syn}), equivalent to one to 20 quanta in order to encompass sparse and clustered activation of parallel fibers (Wilms and Häusser, 2015) at the soma and at 10 µm intervals along the reconstructed dendrites of the immature SC. (Figure 8B). I/O plots showed that sim eEPSPs in the soma and dendrites were less than the linear sum of eEPSPs (dashed line). This sublinear summation was apparent for dendritic eEPSPs generated from synaptic conductances equivalent to 1 quantum for dendritic synapses and became more pronounced for distal synapses (Figure 8C). The sublinearity increased with increasing number of simultaneously activated quanta. These simulations show that immature dendrites demonstrate sublinear summation, supporting experimental difference between somatic and dendritic STP (Figure 8A).

To estimate the impact of development changes in synapse distribution on the maturation of SC computations, we compared simulated subthreshold I/Os between immature and adult SCs with their respective age-dependant g_{syn} (Figure 8C). For immature SCs we examined

subthreshold I/Os when activating synapses at 15 µm along reconstructed dendrites (Figure 8C, green), a distance with the highest relative number of synaptic contacts (Figure 7B), and compared to I/Os generated from synapse activation at 45 µm in adult SCs (distance with the largest relative number of synapses). Sublinearity was quantified by normalizing sim eEPSPs to an sim eEPSP evoked by injecting a g_{syn} of 0.1 quanta, a conductance to which the voltage is linearly related. Because large g_{syn} can generate sublinear integration at the soma (Figure 8C), we estimated the dendrite-specific sublinearity for each g_{syn} by taking the ratio between the relative sim eEPSPs amplitude (normalized to quanta) at a given distance and the normalized sim eEPSP amplitude for somatic synapses. The final estimate of dendritic sublinearity was then defined as one minus this ratio (Figure 8D). While both immature and adult SCs exhibited sublinear integration, dendritic sublinearity was larger in adult SCs for all synaptic strengths, supporting an increased difference between the two layers of integration (i.e. soma versus dendrite). The smaller difference in sublinearity between soma and dendrite in the immature SC resulted from both fewer distal synapses and the larger g_{syn}. Thus the developmental increase in dendritic field complexity and decreased synaptic strength together contribute to the establishment of a two-stage integration model and provide a cellular substrate for a developmental increase in computational power of SCs.

Discussion

Dendritic integration of synaptic inputs is a critical component of neuronal information processing, but little is known about how it matures during neuronal network formation and maturation. We took advantage of the late development of the cerebellar cortex to characterize developmental changes in synaptic and dendritic properties. By combining patch-clamp recording of cerebellar SC interneurons, 3D-reconstructions of their aspiny dendrites, along with the identification of excitatory synapse locations, and numerical simulations, we showed for the first time how the maturation of synapse distribution within interneurons combines with changes in synaptic strength and increased dendritic branching to shape the development of neuronal computation. This maturation process favors the emergence of a compartmentalized two-stage integrator model, which extends the repertoire of transformations of synaptic inputs into neuronal output in adult SCs. These results highlight the importance of characterizing not only dendritic morphology, but also synapse placement and synaptic strength, in order to correctly infer a neuron's computational rules.

Implications of developmental alterations of dendritic morphology

We showed that soon after SC integration into the cerebellar molecular layer microcircuit, their dendrites are nearly the same diameter as adult SCs (Abrahamsson et al., 2012), suggesting a similar capacity for cable filtering of synaptic responses. Since previous studies

suggested that SCs were electronically compact (Carter and Regehr, 2002; Llano and Gerschenfeld, 1993), the observation that mEPSCs from adult SCs were slower led us to consider changes in cable filtering as the underlying mechanism for the developmental change in mEPSC kinetics. However, we showed, both experimentally and by modeling, that dendrite-evoked qEPSCs from immature SCs have similar dendritic integration properties as adult SCs (Abrahamsson et al., 2012): (a) dendrite-evoked qEPSCs are smaller and slower than those evoked at the soma (Figure 3), consistent with cable filtering; (b) STP differed between dendrite and somatic stimulation (Figure 8); and (c) subthreshold I/Os were sublinear (Figure 8). Thus the basic electrotonic machinery to filter synaptic responses is already present as soon as SC precursors reach their final location in the outer third of the molecular layer. However, the maturational difference between mEPSCs, which presumably reflect synaptic responses from the entire dendritic tree, suggested that another factor must be contributing to the difference in apparent electrotonic filtering.

Previous studies have shown that synapses are not uniformly distributed along dendrites, allowing pyramidal neuron dendrites to operate as independent computational units(Katz et al., 2009; Menon et al., 2013; Polsky et al., 2004), and retinal starburst amacrine interneurons to compute motion direction (Vlasits et al., 2016). We considered the possibility that the distribution of synapse locations within the dendritic tree was altered during SC maturation. We found that synapses were uniformly distributed along the somato-dendritic axis with a similar density at the two ages. However, adult SCs had more synapses located at further electrotonic distances (~ 2/3 *vs.* 1/3 of synapses were more than 30 µm from the soma; Figure 6 and 7) due to increased dendritic branching. Thus, the distal-weighted synaptic distribution in adult SCs favors inputs that experience stronger cable filtering. This was confirmed by simulating a mean mEPSC at the two ages, that fully reproduce the mEPSC recorded experimentally (Figure 1), by weighting simulated qEPSCs according to the relative number of synapses at specific distances along the dendrites (Figure 7). Indeed, the large fraction of distal synapses in adult SCs was sufficient to account for the observed developmental difference in mEPSC amplitude and time-course.

Synaptic conductance does not display distance-dependence synaptic scaling

Voltage-clamp recordings of mEPSCs showed that their time course and amplitude are both halved during development (Figure 1). This result contrasts with findings in other neurons that show faster mEPSCs during maturation due to changes of AMPAR subunits, glutamate vesicular concentration content, and/or synapse structure (Cathala et al., 2005; Yamashita et al., 2003). Knowing that dendritic inputs could be electrotonically filtered, we took advantage of the ability to selectively stimulate somatic synapses to isolate somatic qEPSCs for comparison between the two ages. Evoked qEPSCs showed a developmental reduction in

amplitude (~ 40%), with no change in kinetics (Figure 4). This likely results from the smaller adult PSD size (Figure 4), and hence a lower AMPAR number (Masugi-Tokita et al., 2007), rather than a developmental reduction in the peak glutamate concentration at the postsynaptic AMPARs (Figure 1). Therefore individual synaptic inputs are less likely to influence adult SC neuronal output. Moreover, since PSD area is constant along the somato-dendritic axis (Figure 3), the observed developmental reduction in synaptic conductance can be extrapolated to the whole dendritic tree. Thus SCs do not exhibit synaptic conductance scaling mechanisms to offset dendritic filtering, such has been described for pyramidal neurons (Katz et al., 2009; Magee and Cook, 2000; Menon et al., 2013; Nicholson et al., 2006), resulting in a strong dependence of somatic voltage responses on synapse location within the dendritic arbor.

Developmental changes in computational rules

Our findings highlight the critical importance of understanding both the structural and functional mechanisms underlying developmental refinement of synaptic integration that drives a neuron's computational properties and, the emergence of mature microcircuit function. While a defining feature of immature SCs is the high propensity of quantal EPSPs to generate spikes (Carter and Regehr, 2002), the observed developmental decrease in synaptic conductance (Figure 4) and increased filtering of mEPSCs (Figures 2 and 3) will tend to reduce the influence of single synaptic inputs on somatic voltage in adult SCs, increasing their dynamic range of subthreshold integration. Although dendrites in immature and adult SCs exhibit similar electrotonic filtering, the distal bias in synapse location promotes sublinear subthreshold dendritic integration in adult SCs. Unlike pyramidal neurons, where synapse strength and density are scaled to normalize the contribution of individual inputs to neuronal output (Katz et al., 2009; Magee and Cook, 2000; Menon et al., 2013), the spatially uniform distribution of synapse strength and density in SCs do not compensate the electrotonic filtering effects of the dendrites or the increased number of distal synapses due to branching.

These properties of quantal synaptic responses, together with the larger difference in sublinearity between soma and dendrites (Figure 8D), will favor the emergence of a spatially compartmentalized two-stage integration model in adult SCs, thereby promoting location-dependent integration within dendritic subunits (Polsky et al., 2004) and enhanced neuronal computations (Caze et al., 2013). In immature SCs, the repertoire of computations is more similar to a simple single-stage integration model where large and fast synaptic potentials will promote reliable and precise EPSP-spike coupling (Cathala et al., 2003; Fricker and Miles, 2001; Hu et al., 2010), which may be critical for driving the functional maturation of the local microcircuit (Akgül et al., 2020). In contrast, synaptic integration and summation in

adult SCs can obey different rules depending on synapse location within the dendritic tree enabling to discriminate a larger number of spatial patterns of synaptic activation (Tran-Van-Minh et al., 2015) and therefore favor spatially sparse synaptic representations (Abrahamsson et al., 2012; Caze et al., 2013) that might be essential for the development of enhanced pattern separation by Purkinje cells (Cayco-Gajic et al., 2017). Since a recent theoretical study showed that sublinear integration is also a property of hippocampal fast-spiking interneurons (Tzilivaki et al., 2019) that influence memory storage, it will also be important to determine if these interneurons exhibit a similar maturation of their neuronal computation.

Implications for neurodevelopmental and neurological disorders

The increasing complexity of dendritic arbors, accompanying changes in synaptic connectivity and function during development is not limited to the cerebellum. These maturational processes are altered in neurodevelopmental disorders, such as mental retardation (Kaufmann and Moser, 2000), autism spectrum disorders (Antoine et al., 2019; Peng et al., 2016), or Rett Syndrome (Blackman et al., 2012; Ip et al., 2018), as well as in neurodegenerative disease. Indeed, these developmental processes are particularly relevant for interneurons since they play a pivotal role in the establishment of the correct excitation/inhibition balance for normal circuit function. During development, inhibitory interneurons are essential for defining critical periods (Gu et al., 2016; Hensch et al., 1998) or direction selectivity in the retina (Vlasits et al., 2016; Wei et al., 2011), so that interneuron dysfunction is associated with neurodevelopment disorders (Akerman and Cline, 2007; Le Magueresse and Monyer, 2013; Marín, 2016). Our work demonstrates how developmental changes in neuronal morphology, and synapse distribution and strength, combine to determine the impact of synaptic inputs on neuronal output. Our findings provide a functional template of how dendritic integration matures throughout development to enrich interneurons with more complex neuronal computations, promoting location-dependent integration within dendritic subunits.

Materials and Methods

Slice preparation and Electrophysiology

Acute cerebellar parasagittal slices (250 or 200 µm thick respectively) were prepared from immature (postnatal day 14-17) and adult (P35-57) mice (F1 of BalbC and C57B6 or C57BL/6J) as described previously (Abrahamsson et al., 2012). Briefly, mice were killed by decapitation, the brains rapidly removed and placed in an ice-cold solution containing (in mM): 2.5 KCl, 0.5 $CaCl_2$, 4 $MgCl_2$, 1.25 NaH_2PO_4, 24 $NaHCO_3$, 25 glucose, and 230 sucrose, bubbled with 95% O_2 and 5% CO_2. Slices were cut from the dissected cerebellar vermis using a vibratome (Leica VT 1000S or VT1200S), incubated at 32°C for 30 minutes in the following solution (in mM): 85 NaCl, 2.5 KCl, 0.5 $CaCl_2$, 4 $MgCl_2$, 1.25 NaH_2PO_4, 24 $NaHCO_3$, 25 glucose, and 75 sucrose and subsequently maintained at room temperature for up to 8 hours in the recording solution containing (in mM): 125 NaCl, 2.5 KCl, 2 $CaCl_2$, 1 $MgCl_2$, 1.25 NaH_2PO_4, 25 $NaHCO_3$, and 25 glucose. Unless otherwise noted, this solution included during patch recordings 10 µM SR-95531, 10 µM D-AP5, 20 µM 7-chlorokynurenic acid, and 0.3 µM strychnine, to block $GABA_A$, NMDA, and glycine receptors, respectively.

Whole-cell patch-clamp recordings were made from SCs located in the outer one-third at molecular layer at temperatures ranging from 33 to 36°C using an Axopatch-200A or a Multiclamp 700 amplifier (Axon Instruments, Foster City, Ca, USA) with fire-polished thick-walled glass patch-electrodes (tip resistances of 6-8 MΩ) that were backfilled with a solution containing (in mM): 117 K-$MeSO_4$, 40 HEPES, 6 NaOH, 5 EGTA, 1.78 $CaCl_2$, 4 $MgCl_2$, 1 QX-314-Cl, 0.3 NaGTP, 4 NaATP, and, when applied 0.03 Alexa 594, adjusted to ~300 mOsm and pH 7.3. Series resistance and capacitance measures were determined directly from the amplifier settings.

All EPSCs were recorded at -70 mV (not corrected for LJP ~ +6 mV) were filtered at 10 kHz, and digitized at 100 kHz using an analogue-to-digital converter (model NI USB 6259, National Instruments, Austin, TX, USA) and acquired with Nclamp (Rothman and Silver, 2018) within the Igor Pro 6.2 environment, WaveMetrics). No series resistance compensation was used. To evoke EPSC, parallel fibers were stimulated with a glass patch electrode filled with external recording solution that was placed close to a fluorescently labeled dendrite or close to the soma. 50 µs pulses between 5-55 V (Digitimer Ltd, Letchworth Garden City, UK) were delivered as described previously (Abrahamsson et al., 2012). Somatic and dendritic quantal EPSCs were obtained from experiments where [Ca^{2+}] was lowered to 0.5 mM while [Mg^{2+}] was increased to 5 mM to obtain an evoked EPSC success rate <10% known to produce a qEPSC with a <10% amplitude error (Silver, 2003). Trials with a synaptic event could be clearly selected by eye. The stimulation artifact was removed by subtracting from single success traces the average obtained for the traces with

failed synaptic transmission.

Current-clamp recordings were performed using a Multiclamp 700 amplifier. Patch electrodes were coated with dental wax and series resistance was compensated by balancing the bridge and compensating pipette capacitance. Current was injected to maintain the resting potential near -70 mV. Data were filtered at 10 kHz, and digitized at 100 kHz.

D-AP5, 7-chlorokynurenic acid, γDGG, QX-314 chloride, SR 95531 and Tetrodotoxin were purchased from Ascent Scientific (http://www.ascentscientific.com). Alexa 594 was purchased from Invitrogen (https://www.thermofisher.com/invitrogen). All other drugs and chemicals were purchased from Sigma-Aldrich (https://www.sigmaaldrich.com).

Multi-compartmental biophysical modeling

Passive cable simulations of EPSC and EPSP propagation within idealized and reconstructed SC models were performed using Neuron 7.1, 7.2 and 7.5 (Hines and Carnevale, 1997). The idealized SC model had a soma diameter of 9 µm and three 90 µm long dendrites of 0.47 µm diameter, with either 1, 3 or 5 branches. An immature (P16) and adult SC (P42) were reconstructed in 3D with NeuronStudio (Rodriguez et al., 2008) from 2PLSM image of SC patch loaded with 30 µM Alexa 594 in the pipette and imported in Neuron. Passive properties were assumed uniform across the cell. Specific membrane capacitance (C_m) was set to 0.9 µF/cm^2. R_m was set to 20 000 Ωcm^2 to match the membrane time constant experimentally estimated at 19 ± 2.2 ms for immature SCs (n = 16) and 17 ± 2.7 ms for adult SC (n=10). R_i was set to 150 Ωcm to match the filtering of EPSC decay in the dendrites of mature SC (Abrahamson et al., 2012) and allowed to vary from 100 to 200 Ωcm to sample a large range of physiological R_i since its physiological value is not known. The AMPAR-mediated conductance waveforms (gSyn) were set to match the amplitude and kinetics of experimental somatic qEPSCs and evoked EPSCs. Experimental somatic PPR for EPSCs were reproduced with a gSyn2/gSyn1 of 2.25.

Electron microscopy and three-dimensional reconstructions

Electron microscopy and three-dimensional (3D) reconstructions of two SCs from acute slices (postnatal day 14 and 17) were performed as described previously (Abrahamsson et al., 2012). Slices containing SCs whole-cell patched with a K-MeSO3-based internal solution containing biocytin (0.3%) and Alexa 594 (30 µM) were transferred to a fixative containing paraformaldehyde (2.5%), glutaraldehyde (1.25%), and picric acid (0.2%) in phosphate buffer (PB, 0.1 M, pH = 7.3), and fixed overnight at room temperature. After washing in PB, slices were transferred to sucrose solutions (15% for 30 minutes, then stored in 30%) for cryoprotection and frozen in liquid nitrogen, then subsequently thawed. The freeze-thaw

cycle was repeated twice, then followed by incubation with a 1.4nm gold-conjugated streptavidin (Nanoprobe, 1:100 in Tris-buffered saline (TBS) and 0.03% Triton X100). After washing in TBS and dH_2O, slices were treated with HQ silver enhancement kit (Nanoprobe) for 5 minutes, fixed in 1% OsO4 in PB for 30 minutes, and block stained with 1% uranyl acetate for 40 minutes. After dehydration through a series of ethanol solutions (50, 70, 80, 90, 95, 99, and 100%) and propylene oxide twice for 10 minutes, slices were embedded into Durcupan (Fluka) and flat embedded. The labeled SCs were trimmed and 300~400 serial ultrathin sections were cut at 70 nm using ATUMtome (RMC Boeckeler). Serial sections containing immunogold labeled profiles were imaged with a scanning electron microscope (Merlin Compact, Zeiss) and Zeiss Atlas package at X 22,000 for whole-cell reconstruction and at X 55,000 for synapses. For the area measurement of synapses on soma, serial sections through three unlabeled neighbor SCs were also used to avoid potential turbulence due to the patching. These sections were cut at 70 nm using an ultramicrotome (Leica EM UC7), observed with a transmission electron microscope (Tecnai 12, FEI), and photographed at X 21,000. Asymmetrical synapses made by axon terminals onto SC somata and dendrites were analyzed only if they were fully present within the serial sections. The PSD length of the asymmetrical synaptic membrane specialization was measured on each ultrathin section, and the PSD area was calculated by multiplying the summed synaptic length from each synapse with the thickness (70 nm) of the ultrathin sections. The 3D reconstruction of the two SC soma and parts of their dendritic trees was performed using the software Reconstruct (JC Fiala). The distances from each synapse to the soma were measured along the dendrites in the reconstructed volume.

Transmitted light and fluorescence imaging

SC somata in the outer one-third of the molecular layer were identified and whole-cell patched using infrared Dodt contrast (Luigs and Neumann). Two-photon excitation or LED illumination coupled with the Dodt contrast was used to visualize Alexa 594 filled SCs and position extracellular stimulating electrodes along isolated dendrites of SCs fluorescence. Two-photon excitation was performed with a pulsed Ti:Sapphire laser (MaiTai DeepSee, Spectra Physics) tuned to 810 nm and images were acquired with an Ultima two-photon laser scanning microscope system (Bruker) mounted on an Olympus BX61WI microscope equipped with a 60x (1.1 NA) water-immersion objective. LED excitation (470 nm) was performed with a CAIRN LED module (optoLED) and wide-field fluorescence images were acquired with a CCD camera (QIclick, QImaging) mounted on an Olympus BX51 microscope equipped with a 60x (1 NA) water-immersion objective.

One-photon confocal laser scanning fluorescence microscopy was performed with an Ultima scan head mounted on a Nikon EFN microscope. SCs were filled with 40 µM Alexa 488.

Maximal intensity projections of confocal images were performed using a 100x 1.1 NA Nikon dipping objective in 0.2 µm increments as described previously (Abrahamsson et al., 2012). We used the full-width at half maximum (FWHM) of intensity line profiles on 1 µm segments of dendrites, made perpendicular to dendritic length, as an approximation of the dendritic diameter. This is likely to be an upper limit given the blurring effect of the PSF.

2P imaging: The two-photon scanning microscope (2PLSM, Ultima IV, Bruker) was equipped with a Ti:Sapphire Laser (Chameleon II, Coherent Inc.) at 940nm (SC body, Alexa 594) and 810nm (venus-tagged PSD95 puncta) using a 60x water immersion objective (LUMFL N, 1.10 NA, Olympus). The point spread function of the microscope was estimated from the FWHM value of the x-,y- and z- intensity line profiles from 3D images of 200nm yellow-green fluorescent latex beads (FluoSpheres, F8811, Thermo Fisher Scientific): $PSF_{810x/y}$ = 325 ± 27 (SD) nm, PSF_{810z} =1178 ± 121(SD) nm, and $PSF_{940x/y}$ = 390 ± 23 (SD), PSF_{940z} =1412 ± 141 (SD) nm.

Three-dimensional reconstructions and puncta detection from 2P images

We examined the distribution of excitatory synaptic inputs along the somato-dendritic compartment in SCs from a transgenic mouse line that conditionally expresses Venus-tagged PSD95 under the control of the nitric oxide synthase 1 promoter (PSD95-Enabled (Fortin et al., 2014) x Nos1 Cre (Kim et al., 2014)). We patch-loaded single SCs with the fluorescence indicator Alexa 594, then performed live two-color 2PLSM to identify Venus-tagged PSD95 puncta associated with the labeled somata and dendritic trees. Z-stacks were acquired for each wavelength with a z-step of 300 nm, a pixel size of 154 nm, and an image size of 512 x 512 pixels. To correct for a shift in the focal point for the different wavelengths and a potential drift in x/y-directions, the individual stacks were registered to each other using as a reference the dendritic structure imaged using Alexa 594 emission, which is primarily excited at 810 nm, but weakly excited at 940 nm which allows to record both the puncta and the cell body simultaneously. The registration was performed using the IMARIS *stitcher* tool. Fluorescence emission was spectrally separated from laser excitation using a custom multi-pass dichroic (zt 405/473-488/nir-trans; Chroma) and a short pass IR blocking filter (ET680sp-2p8; Chroma). Venus and Alexa 594 fluorescence emission were spectrally separated and detected using detection filter cubes consisting of a long-pass dichroic (575dcxr; Chroma) and two bandpass filters (HQ525/70m-2p and HQ607/45m-2p, respectively; Chroma). A multi-alkali (R3896, Hamamatsu, Japan) photomultiplier tubes was used to detect Alexa 594 fluorescence and gallium arsenide phosphide tube (H7422PA-40 SEL, Hamamatsu) for the Venus channel. Proximal and substage detection were used to increase signal to noise.

Dendrite tracing: The image analysis software IMARIS 9.5 (Bitplane) was used for dendritic tracing and fluorescence puncta detection. Fluorescence images were filtered using a 3x3 px median filter to remove noise. Image stacks were then further combined using the IMARIS *stitcher* tool to create one contiguous file that permits tracing of the entire dendritic tree. Dendrites, but not axons, were traced in IMARIS using the *filament* tool in a semi-automatic mode using the *AutoPath* method and the options *AutoCenter* and *AutoDiameter* activated. The soma center was chosen as the starting point with centripetally tracing along dendrites. Dendritic lengths were estimated as the dendritic path distance from the center of the soma and Sholl analysis was performed with IMARIS from all reconstructed SC.

PSD-95 Venus puncta detection: Fluorescence puncta were detected using the IMARIS spot creation tool, using background fluorescence subtraction to compensate for different levels of fluorescent intensity along the z-axis of the stack. The initial minimal spot search size was set to 300x300x1100 nm, slightly smaller than the PSF at 810 nm. No further thresholds or criteria were applied inside IMARIS. Parameters describing the fluorescent puncta, including the intensity at the center, their spatial coordinates, and their diameters, were exported as excel files via the Statistics tab and further analyzed using custom python scripts. In order to separate the PSD95 puncta from false detection of noise, two threshold criteria were applied. 1) All spots with a diameter smaller than and equal to the PSF (300x300x1100nm) were rejected. 2) Only spots with a peak intensity larger than the mean of the background intensity plus three times its standard deviation of the background noise, were considered for subsequent analysis. In combination, the thresholds ensure that the spots originated from fluorescent puncta and not false positives generated from noise fluctuations. The background intensity and its corresponding standard deviation was measured for each file in *Fiji*, by selecting regions without puncta and using the *Measure* tool to calculate the mean and standard deviation. In order to ensure consistent sampling of the background, mean and noise estimates were made from at least ten different regions at different z positions in each stack, corresponding to an area between 17-27 μm^2 (790 - 1210 pixels) and 10 - 40 μm^2 (430 - 1850 pixels), for the immature and adult SCs, respectively. This approach is limited by the resolution of 2P fluorescence imaging to differentiate individual synapses within clusters and thus may result in an underestimate of absolute synapse density, but allowed for an unbiased estimate of synapse distributions at the two developmental stages.

Puncta located on somata were selected from the total pool of detected puncta (described above) using the following criteria: 1) spots were associated with the soma if the peak intensity at the position of the spot center in the Alexa 594 channel was larger than half the maximum of the whole stack, 2) detected spot diameters were greater than the size PSF (300x300x1100nm), 3) spot intensities were larger than the mean plus 3*SD of background intensity of the PSD95-venus channel, measured from within the soma. Puncta from somata

that showed saturation in the Alexa 594 channel were not included in the analysis.

Analysis of spot and dendrite distances: The structure of the dendritic tree, as well as the position of the puncta, were further analyzed using custom python scripts. The dendritic tree was reconstructed with the center of the soma as its root using the python *NetworkX* package. Fluorescence puncta were considered to arise from the labeled dendrite if they were located within a maximal distance from the center of the dendrite. This distance was taken as the dendritic radius, estimated from IMARIS, plus 200 nm (~HWHM of the PSF_{810}). The estimation of local radius was made from IMARIS binary masks using a threshold of the local contrast (*DiameterContrastThreshold)* set at three times the standard deviation above the background fluorescence noise. The diameter is then calculated using the *Shortest Distance from Distance Map* algorithm, which estimates the diameter as the distance from the center of the dendrite to the closest part of the surface determined by the above threshold. The average dendritic radius, using this approach, was found to be 0.66 ± 0.28 (SD) µm for adult, and 0.72 ± 0.27 (SD) µm for immature mice. As this value was larger than that estimated from single-photon confocal imaging, it was only used as a part of the criteria for assigning a fluorescence puncta to a reconstructed dendrite. For each dendritic branch, the number of PSD95 puncta and their distance to the soma surface were calculated. As the data points of the dendrite structure obtained from IMARIS are not homogeneously spaced, the dendritic structure was resampled in 100 nm intervals with the distance for each segment recalculated with respect to the starting point of each corresponding branch from the soma surface (estimated using the binary mask as for the dendrites). Histograms for the distribution of PSD95 puncta and the number of dendritic segments at a given distance from the soma were then generated in 10µm bins and used to estimate the puncta density along the dendritic tree. Cumulative plots were sampled at 1µm intervals.

Electrophysiology analysis

Data analysis was performed using the Neuromatic analysis package (Rothman and Silver, 2018) written within the Igor Pro environment (WaveMetrics, Lake Oswego, OR, USA). mEPSCs were detected with a threshold detection method and mEPSC population average is calculated from the mean EPSC response calculated for each SC. All EPSC were baseline subtracted using a 1 ms window before the stimulation artifact. Peak amplitudes were measured as the difference between the baseline level immediately preceding the stimulation artifact, and the mean amplitude over a 100 µs window centered on the peak of the response. EPSC decay kinetics were assessed either as the width of the EPSC at the amplitude one-half of the peak (half-width in ms) or as the weighted time constant of decay (τ_{decay}) calculated from the integral of the current from the peak, according to:

$$t_{decay} = \frac{\int_{t_{peak}}^{t_\infty} I(t)\,dt}{I_{peak}}$$

where t_{peak} is the time of the EPSC peak, t_∞ is the time at which the current had returned to the pre-event baseline, and I_{peak} the peak amplitude of the EPSC.

All data are expressed as average ± SEM otherwise noted. Statistical tests were performed using a nonparametric Wilcoxon-Mann-Whitney two-sample rank test routine for unpaired or a Wilcoxon signed-rank test routine for paired comparisons. Kolmogorov–Smirnov test (KS test) was used to compare cumulative distributions. Unless otherwise noted, unpaired tests were used and considered significant at $P<0.05$ (OriginPro, Northampton, MA, USA)

Equation 1. Length constant for an infinite cable.

$$\lambda_{DC} = \sqrt{\frac{dR_m}{4R_i}},$$

where d is the dendritic diameter and R_m and R_i are the specific resistance of the membrane and internal resistivity, respectively.

Equation 2. Frequency-dependent length constant for an infinite cable.

$$\lambda_{AC} = \lambda_{DC}\sqrt{\frac{2}{1+\sqrt{1+(2\pi f\tau_m)^2}}},$$

where f is the frequency representing an AMPAR current and τ_m is the membrane time constant.

When f is greater than 100 Hz, this can be simplied when f is greater than 100 Hz:

$$\lambda_{AC} \approx \sqrt{\frac{d}{4\pi f R_i C_m}}$$

Acknowledgements:

This study was supported by the Centre National de la Recherche Scientifique and the Agence Nationale de la Recherche (ANR-13-BSV4-00166, to LC and DAD). TA was supported by fellowships from the Fondation pour la Recherche Medicale and the Swedish Research Council. We thank Dmitry Ershov from the Image Analysis Hub of the Institut Pasteur, Elodie Le Monnier, Elena Hollergschwandtner, Vanessa Zheden and Corinne Nantet for technical support and Haining Zhong for providing the Venus-tagged PSD95 mouse line. We would like to thank Alberto Bacci, Ann Lohof and Nelson Rebola for comments on the manuscript.

Competing interests:

The authors have no competing financial or non-financial interests.

References

Abrahamsson T, Cathala L, Matsui K, Shigemoto R, DiGregorio DA. 2012. Thin dendrites of cerebellar interneurons confer sublinear synaptic integration and a gradient of short-term plasticity. *Neuron* **73**:1159–72. doi:10.1016/j.neuron.2012.01.027

Akerman CJ, Cline HT. 2007. Refining the roles of GABAergic signaling during neural circuit formation. *Trends Neurosci* **30**:382–389. doi:10.1016/j.tins.2007.06.002

Ango F, di Cristo G, Higashiyama H, Bennett V, Wu P, Huang ZJ. 2004. Ankyrin-based subcellular gradient of neurofascin, an immunoglobulin family protein, directs GABAergic innervation at purkinje axon initial segment. *Cell* **119**:257–272. doi:10.1016/j.cell.2004.10.004

Antoine MW, Langberg T, Schnepel P, Feldman DE. 2019. Increased Excitation-Inhibition Ratio Stabilizes Synapse and Circuit Excitability in Four Autism Mouse Models. *Neuron* **101**:648-661.e4. doi:10.1016/j.neuron.2018.12.026

Arlt C, Häusser M. 2020. Microcircuit Rules Governing Impact of Single Interneurons on Purkinje Cell Output In Vivo. *Cell Rep* **30**:3020-3035.e3. doi:10.1016/j.celrep.2020.02.009

Ben-Ari Y. 2002. Excitatory actions of gaba during development: the nature of the nurture. *Nat Rev Neurosci* **3**:728–739. doi:10.1038/nrn920

Blackman MP, Djukic B, Nelson SB, Turrigiano GG. 2012. A critical and cell-autonomous role for MeCP2 in synaptic scaling up. *J Neurosci Off J Soc Neurosci* **32**:13529–13536. doi:10.1523/JNEUROSCI.3077-12.2012

Bloomfield SA, Hamos JE, Sherman SM. 1987. Passive cable properties and morphological correlates of neurones in the lateral geniculate nucleus of the cat. *J Physiol* **383**:653–692. doi:10.1113/jphysiol.1987.sp016435

Bloss EB, Cembrowski MS, Karsh B, Colonell J, Fetter RD, Spruston N. 2018. Single excitatory axons form clustered synapses onto CA1 pyramidal cell dendrites. *Nat Neurosci* **21**:353–363. doi:10.1038/s41593-018-0084-6

Branco T, Häusser M. 2011. Synaptic integration gradients in single cortical pyramidal cell dendrites. *Neuron* **69**:885–892. doi:10.1016/j.neuron.2011.02.006

Carter AG, Regehr WG. 2002. Quantal events shape cerebellar interneuron firing. *Nat Neurosci* **5**:1309–18.

Cathala L, Brickley S, Cull-Candy S, Farrant M. 2003. Maturation of EPSCs and intrinsic membrane properties enhances precision at a cerebellar synapse. *J Neurosci* **23**:6074–85.

Cathala L, Holderith NB, Nusser Z, DiGregorio DA, Cull-Candy SG. 2005. Changes in synaptic structure underlie the developmental speeding of AMPA receptor-mediated EPSCs. *Nat Neurosci* **8**:1310–8.

Cayco-Gajic NA, Clopath C, Silver RA. 2017. Sparse synaptic connectivity is required for decorrelation and pattern separation in feedforward networks. *Nat Commun* **8**:1116. doi:10.1038/s41467-017-01109-y

Caze RD, Humphries M, Gutkin B. 2013. Passive dendrites enable single neurons to compute linearly non-separable functions. *PLoS Comput Biol* **9**:e1002867. doi:10.1371/journal.pcbi.1002867

Chen C, Regehr WG. 2000. Developmental remodeling of the retinogeniculate synapse. *Neuron* **28**:955–966. doi:10.1016/s0896-6273(00)00166-5

Cline HT. 2016. Dendrite developmentDendrites. Oxford University press. pp. 77–94.

Diamond JS, Jahr CE. 1997. Transporters buffer synaptically released glutamate on a submillisecond time scale. *J Neurosci Off J Soc Neurosci* **17**:4672–4687.

Fortin DA, Tillo SE, Yang G, Rah JC, Melander JB, Bai S, Soler-Cedeno O, Qin M, Zemelman BV, Guo C, Mao T, Zhong H. 2014. Live imaging of endogenous PSD-95 using ENABLED: a conditional strategy to fluorescently label endogenous proteins. *J Neurosci* **34**:16698–712. doi:10.1523/JNEUROSCI.3888-14.2014

Foster KA, Crowley JJ, Regehr WG. 2005. The influence of multivesicular release and postsynaptic receptor saturation on transmission at granule cell to Purkinje cell synapses. *J Neurosci Off J Soc Neurosci* **25**:11655–11665. doi:10.1523/JNEUROSCI.4029-05.2005

Fricker D, Miles R. 2001. Interneurons, spike timing, and perception. *Neuron* **32**:771–774. doi:10.1016/s0896-6273(01)00528-1

Gidon A, Zolnik TA, Fidzinski P, Bolduan F, Papoutsi A, Poirazi P, Holtkamp M, Vida I, Larkum ME. 2020. Dendritic action potentials and computation in human layer 2/3 cortical neurons. *Science* **367**:83–87. doi:10.1126/science.aax6239

Grillo FW, Neves G, Walker A, Vizcay-Barrena G, Fleck RA, Branco T, Burrone J. 2018. A Distance-Dependent Distribution of Presynaptic Boutons Tunes Frequency-Dependent Dendritic Integration. *Neuron* **99**:275-282.e3. doi:10.1016/j.neuron.2018.06.015

Gu Y, Tran T, Murase S, Borrell A, Kirkwood A, Quinlan EM. 2016. Neuregulin-Dependent Regulation of Fast-Spiking Interneuron Excitability Controls the Timing of the Critical Period. *J Neurosci Off J Soc Neurosci* **36**:10285–10295. doi:10.1523/JNEUROSCI.4242-15.2016

Häusser M, Clark BA. 1997. Tonic synaptic inhibition modulates neuronal output pattern and spatiotemporal synaptic integration. *Neuron* **19**:665–678. doi:10.1016/s0896-6273(00)80379-7

Hensch TK, Fagiolini M, Mataga N, Stryker MP, Baekkeskov S, Kash SF. 1998. Local GABA circuit control of experience-dependent plasticity in developing visual cortex. *Science* **282**:1504–1508. doi:10.1126/science.282.5393.1504

Hestrin S. 1992. Developmental regulation of NMDA receptor-mediated synaptic currents at a central synapse. *Nature* **357**:686–689. doi:10.1038/357686a0

Hu H, Gan J, Jonas P. 2014. Interneurons. Fast-spiking, parvalbumin^{+} GABAergic interneurons: from cellular design to microcircuit function. *Science* **345**:1255263. doi:10.1126/science.1255263

Hu H, Martina M, Jonas P. 2010. Dendritic mechanisms underlying rapid synaptic activation of fast-spiking hippocampal interneurons. *Science* **327**:52–58. doi:10.1126/science.1177876

Ip JPK, Mellios N, Sur M. 2018. Rett syndrome: insights into genetic, molecular and circuit mechanisms. *Nat Rev Neurosci* **19**:368–382. doi:10.1038/s41583-018-0006-3

Katz LC, Shatz CJ. 1996. Synaptic activity and the construction of cortical circuits. *Science* **274**:1133–1138. doi:10.1126/science.274.5290.1133

Katz Y, Menon V, Nicholson DA, Geinisman Y, Kath WL, Spruston N. 2009. Synapse distribution suggests a two-stage model of dendritic integration in CA1 pyramidal neurons. *Neuron* **63**:171–177. doi:10.1016/j.neuron.2009.06.023

Kaufmann WE, Moser HW. 2000. Dendritic anomalies in disorders associated with mental retardation. *Cereb Cortex N Y N 1991* **10**:981–991. doi:10.1093/cercor/10.10.981

Kim J, Lee S, Tsuda S, Zhang X, Asrican B, Gloss B, Feng G, Augustine GJ. 2014. Optogenetic Mapping of Cerebellar Inhibitory Circuitry Reveals Spatially Biased Coordination of Interneurons via Electrical Synapses. *Cell Rep* **7**:1601–1613.

doi:10.1016/j.celrep.2014.04.047

Koike-Tani M, Saitoh N, Takahashi T. 2005. Mechanisms underlying developmental speeding in AMPA-EPSC decay time at the calyx of Held. *J Neurosci* **25**:199–207.

Kwon H-B, Sabatini BL. 2011. Glutamate induces de novo growth of functional spines in developing cortex. *Nature* **474**:100–104. doi:10.1038/nature09986

Larkum ME, Nevian T, Sandler M, Polsky A, Schiller J. 2009. Synaptic integration in tuft dendrites of layer 5 pyramidal neurons: a new unifying principle. *Science* **325**:756–760. doi:10.1126/science.1171958

Lawrence JJ, Trussell LO. 2000. Long-term specification of AMPA receptor properties after synapse formation. *J Neurosci Off J Soc Neurosci* **20**:4864–4870.

Le Magueresse C, Monyer H. 2013. GABAergic interneurons shape the functional maturation of the cortex. *Neuron* **77**:388–405. doi:10.1016/j.neuron.2013.01.011

Li J, Erisir A, Cline H. 2011. In vivo time-lapse imaging and serial section electron microscopy reveal developmental synaptic rearrangements. *Neuron* **69**:273–286. doi:10.1016/j.neuron.2010.12.022

Liu G, Choi S, Tsien RW. 1999. Variability of neurotransmitter concentration and nonsaturation of postsynaptic AMPA receptors at synapses in hippocampal cultures and slices. *Neuron* **22**:395–409. doi:10.1016/s0896-6273(00)81099-5

Llano I, Gerschenfeld HM. 1993. Inhibitory synaptic currents in stellate cells of rat cerebellar slices. *J Physiol Lond* **468**:177–200.

Losonczy A, Magee JC. 2006. Integrative properties of radial oblique dendrites in hippocampal CA1 pyramidal neurons. *Neuron* **50**:291–307. doi:10.1016/j.neuron.2006.03.016

Losonczy A, Makara JK, Magee JC. 2008. Compartmentalized dendritic plasticity and input feature storage in neurons. *Nature* **452**:436–441. doi:10.1038/nature06725

Magee JC. 2000. Dendritic integration of excitatory synaptic input. *Nat Rev Neurosci* **1**:181–190. doi:10.1038/35044552

Magee JC. 1999. Dendritic lh normalizes temporal summation in hippocampal CA1 neurons. *Nat Neurosci* **2**:508–514. doi:10.1038/9158

Magee JC, Cook EP. 2000. Somatic EPSP amplitude is independent of synapse location in hippocampal pyramidal neurons. *Nat Neurosci* **3**:895–903. doi:10.1038/78800

Marín O. 2016. Developmental timing and critical windows for the treatment of psychiatric disorders. *Nat Med* **22**:1229–1238. doi:10.1038/nm.4225

Masugi-Tokita M, Tarusawa E, Watanabe M, Molnar E, Fujimoto K, Shigemoto R. 2007. Number and density of AMPA receptors in individual synapses in the rat cerebellum as revealed by SDS-digested freeze-fracture replica labeling. *J Neurosci* **27**:2135–44.

McBride TJ, Rodriguez-Contreras A, Trinh A, Bailey R, Debello WM. 2008. Learning drives differential clustering of axodendritic contacts in the barn owl auditory system. *J Neurosci Off J Soc Neurosci* **28**:6960–6973. doi:10.1523/JNEUROSCI.1352-08.2008

McCormick DA, Prince DA. 1987. Post-natal development of electrophysiological properties of rat cerebral cortical pyramidal neurones. *J Physiol* **393**:743–762. doi:10.1113/jphysiol.1987.sp016851

Menon V, Musial TF, Liu A, Katz Y, Kath WL, Spruston N, Nicholson DA. 2013. Balanced synaptic impact via distance-dependent synapse distribution and complementary expression of AMPARs and NMDARs in hippocampal dendrites. *Neuron* **80**:1451–1463. doi:10.1016/j.neuron.2013.09.027

Mittmann W, Koch U, Häusser M. 2005. Feed-forward inhibition shapes the spike output of cerebellar Purkinje cells. *J Physiol* **563**:369–378. doi:10.1113/jphysiol.2004.075028

Nevian T, Larkum ME, Polsky A, Schiller J. 2007. Properties of basal dendrites of layer 5 pyramidal neurons: a direct patch-clamp recording study. *Nat Neurosci* **10**:206–214. doi:10.1038/nn1826

Nicholson DA, Trana R, Katz Y, Kath WL, Spruston N, Geinisman Y. 2006. Distance-dependent differences in synapse number and AMPA receptor expression in hippocampal CA1 pyramidal neurons. *Neuron* **50**:431–442. doi:10.1016/j.neuron.2006.03.022

Pelkey KA, Barksdale E, Craig MT, Yuan X, Sukumaran M, Vargish GA, Mitchell RM, Wyeth MS, Petralia RS, Chittajallu R, Karlsson R-M, Cameron HA, Murata Y, Colonnese MT, Worley PF, McBain CJ. 2015. Pentraxins coordinate excitatory synapse maturation and circuit integration of parvalbumin interneurons. *Neuron* **85**:1257–1272. doi:10.1016/j.neuron.2015.02.020

Peng Y, Lu Z, Li G, Piechowicz M, Anderson M, Uddin Y, Wu J, Qiu S. 2016. The autism-associated MET receptor tyrosine kinase engages early neuronal growth mechanism and controls glutamatergic circuits development in the forebrain. *Mol Psychiatry* **21**:925–935. doi:10.1038/mp.2015.182

Penzes P, Cahill ME, Jones KA, VanLeeuwen J-E, Woolfrey KM. 2011. Dendritic spine pathology in neuropsychiatric disorders. *Nat Neurosci* **14**:285–293. doi:10.1038/nn.2741

Poirazi P, Mel BW. 2001. Impact of active dendrites and structural plasticity on the memory capacity of neural tissue. *Neuron* **29**:779–96.

Polsky A, Mel BW, Schiller J. 2004. Computational subunits in thin dendrites of pyramidal cells. *Nat Neurosci* **7**:621–627. doi:10.1038/nn1253

Pouille F, Scanziani M. 2001. Enforcement of Temporal Fidelity in Pyramidal Cells by Somatic Feed-Forward Inhibition. *Science* **293**:1159–1163. doi:10.1126/science.1060342

Rall W. 1967. Distinguishing theoretical synaptic potentials computed for different soma-dendritic distributions of synaptic input. *J Neurophysiol* **30**:1138–1168. doi:10.1152/jn.1967.30.5.1138

Rodriguez A, Ehlenberger DB, Dickstein DL, Hof PR, Wearne SL. 2008. Automated three-dimensional detection and shape classification of dendritic spines from fluorescence microscopy images. *PloS One* **3**:e1997. doi:10.1371/journal.pone.0001997

Rothman JS, Silver RA. 2018. NeuroMatic: An Integrated Open-Source Software Toolkit for Acquisition, Analysis and Simulation of Electrophysiological Data. *Front Neuroinformatics* **12**:14. doi:10.3389/fninf.2018.00014

Sanes DH. 1993. The development of synaptic function and integration in the central auditory system. *J Neurosci Off J Soc Neurosci* **13**:2627–2637.

Schiller J, Major G, Koester HJ, Schiller Y. 2000. NMDA spikes in basal dendrites of cortical pyramidal neurons. *Nature* **404**:285–289. doi:10.1038/35005094

Scholl B, Wilson DE, Fitzpatrick D. 2017. Local Order within Global Disorder: Synaptic Architecture of Visual Space. *Neuron* **96**:1127-1138.e4. doi:10.1016/j.neuron.2017.10.017

Sigler A, Oh WC, Imig C, Altas B, Kawabe H, Cooper BH, Kwon H-B, Rhee J-S, Brose N. 2017. Formation and Maintenance of Functional Spines in the Absence of Presynaptic Glutamate Release. *Neuron* **94**:304-311.e4. doi:10.1016/j.neuron.2017.03.029

Silver RA. 2010. Neuronal arithmetic. *Nat Rev Neurosci* **11**:474–489. doi:10.1038/nrn2864

Taschenberger H, von Gersdorff H. 2000. Fine-tuning an auditory synapse for speed and

fidelity: developmental changes in presynaptic waveform, EPSC kinetics, and synaptic plasticity. *J Neurosci Off J Soc Neurosci* **20**:9162–9173.

Tia S, Wang JF, Kotchabhakdi N, Vicini S. 1996. Developmental changes of inhibitory synaptic currents in cerebellar granule neurons: role of GABA(A) receptor alpha 6 subunit. *J Neurosci Off J Soc Neurosci* **16**:3630–3640.

Tran-Van-Minh A, Caze RD, Abrahamsson T, Cathala L, Gutkin BS, DiGregorio DA. 2015. Contribution of sublinear and supralinear dendritic integration to neuronal computations. *Front Cell Neurosci* **9**:67. doi:10.3389/fncel.2015.00067

Tzilivaki A, Kastellakis G, Poirazi P. 2019. Challenging the point neuron dogma: FS basket cells as 2-stage nonlinear integrators. *Nat Commun* **10**:1–14. doi:10.1038/s41467-019-11537-7

Vervaeke K, Lorincz A, Nusser Z, Silver RA. 2012. Gap junctions compensate for sublinear dendritic integration in an inhibitory network. *Science* **335**:1624–1628. doi:10.1126/science.1215101

Vlasits AL, Morrie RD, Tran-Van-Minh A, Bleckert A, Gainer CF, DiGregorio DA, Feller MB. 2016. A Role for Synaptic Input Distribution in a Dendritic Computation of Motion Direction in the Retina. *Neuron* **89**:1317–1330. doi:10.1016/j.neuron.2016.02.020

Wei W, Hamby AM, Zhou K, Feller MB. 2011. Development of asymmetric inhibition underlying direction selectivity in the retina. *Nature* **469**:402–406. doi:10.1038/nature09600

Williams SR, Stuart GJ. 2002. Dependence of EPSP efficacy on synapse location in neocortical pyramidal neurons. *Science* **295**:1907–1910. doi:10.1126/science.1067903

Wilms CD, Häusser M. 2015. Reading out a spatiotemporal population code by imaging neighbouring parallel fibre axons in vivo. *Nat Commun* **6**:6464. doi:10.1038/ncomms7464

Xu N, Harnett MT, Williams SR, Huber D, O'Connor DH, Svoboda K, Magee JC. 2012. Nonlinear dendritic integration of sensory and motor input during an active sensing task. *Nature* **492**:247–251. doi:10.1038/nature11601

Yamashita T, Ishikawa T, Takahashi T. 2003. Developmental increase in vesicular glutamate content does not cause saturation of AMPA receptors at the calyx of held synapse. *J Neurosci* **23**:3633–8.

Zhang Z. 2004. Maturation of layer V pyramidal neurons in the rat prefrontal cortex: intrinsic properties and synaptic function. *J Neurophysiol* **91**:1171–1182. doi:10.1152/jn.00855.2003

Figure 1

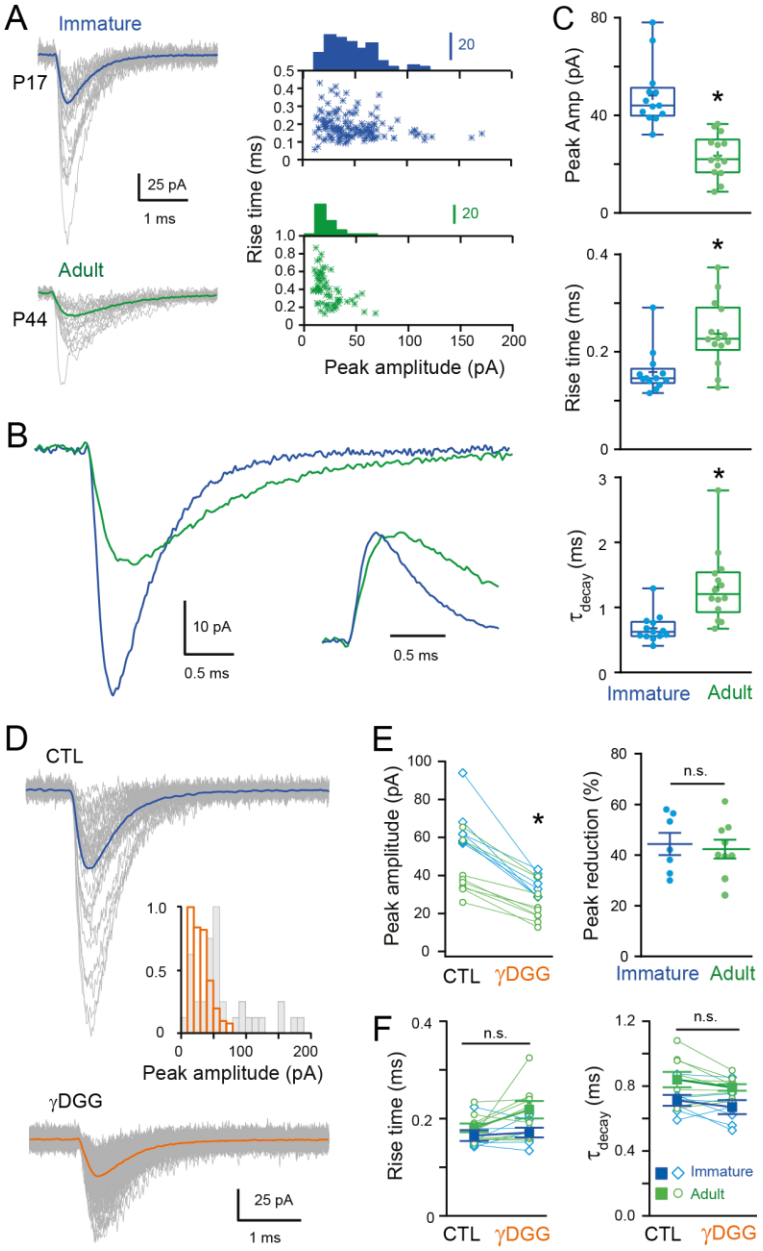

Figure 1. Developmental maturation of the AMPAR-mediated mEPSC in SC. (A) Left panels show superimposed single mEPSCs (grey) and the corresponding average (bold) recorded at -70 mV obtained from a representative immature SCs (P17, blue trace) and adult SCs (P44, green trace). Right panels show corresponding plots of peak amplitude as a function of 10-90% rise time, with the superimposed amplitude distributions. **(B)** Superimposed mEPSC average aligned on event onset. Inset : traces normalized to their peak **(C)** Box and whisker plots showing the median (line) peak amplitude, 10-90% rise time and decay (τ_{decay}) at both ages (PN 17 to 19; 17.4 ± 0.27, days, n = 13 and PN 37 to 57; 45 ± 1.75 days, n = 14, n = 14 respectively), the 25th and 75th percentile (box), range (whiskers) and mean (+). Superimposed filled circles represent individual cells (asterisks denote P<0.05). **(D)** Representative examples of single mEPSC events (grey) and the corresponding average (bold) in control (CTL) and in the presence of γDGG (1 mM). Inset shows the corresponding mEPSC peak amplitude distributions. **(E)** The effect of γDGG on mEPSCs at the two ages (n = 7 and n = 9 respectively): left panel its effect on individual mean peak amplitude for each SC (blue for immature and green for adult SC); and right panel, summary plot showing the % reduction of mEPSC peak amplitude.**(F)** Plot summarizing the effect of γDGG on mEPSC rise time (left panel) and decay (τ_{decay}, right panel) at the two ages for individual cells (open symbols) and on population averages (± SEM)

Figure 2

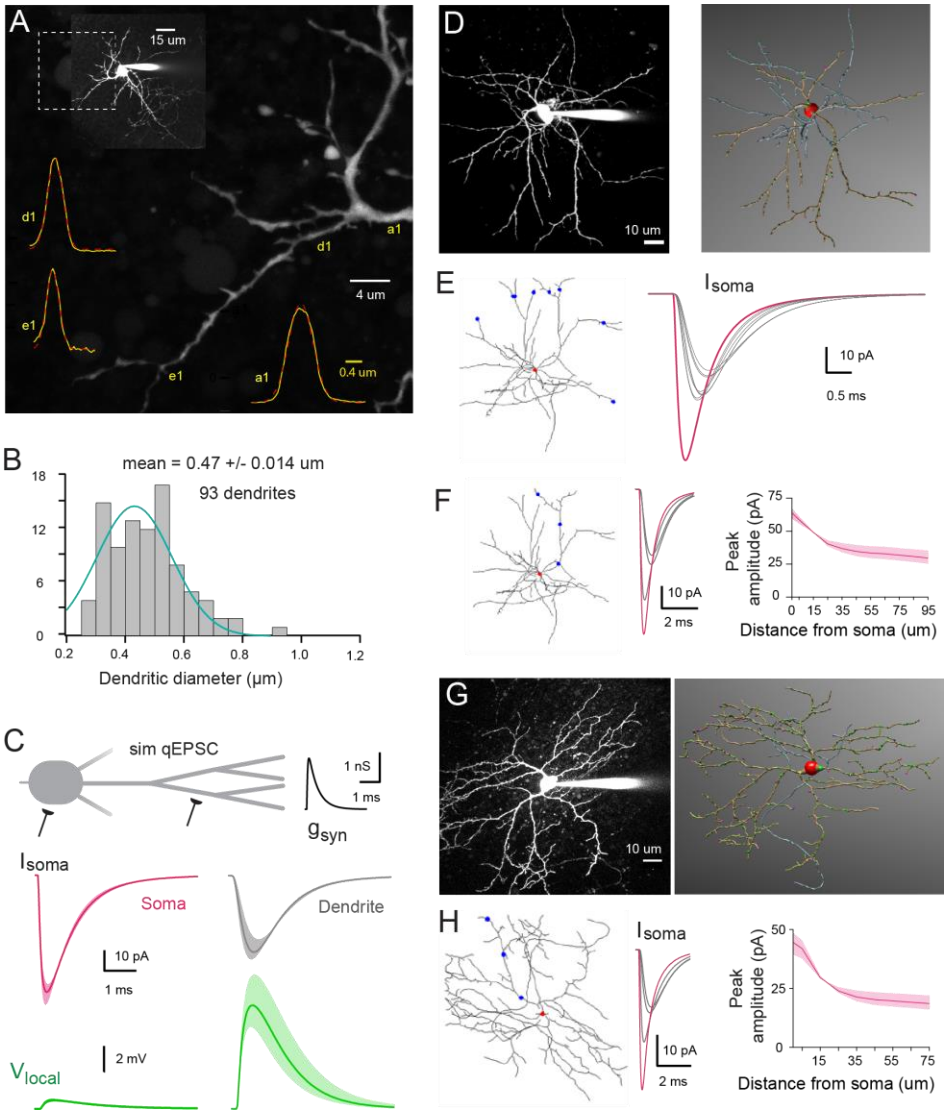

Figure 2. Numerical simulations of SC dendrites indicate significant cable filtering and large local depolarizations in immature SC. (A) Maximal intensity projection of one-photon confocal images of an immature SC labeled with Alexa 488. Examples of intensity profiles (Yellow line) of 3 dendritic locations superimposed on the image. Dendrite diameter is approximated by the full width half maximum (FWHM) of the Gaussian fit of the line profile (broken red line). **(B)** Histogram showing the distribution of dendrite diameters from 93 dendrites, with a Gaussian fit indicating a mode centered at 0.43 ± 0.008 µm. **(C)** Numerical simulations of somatic qEPSCs in a passive neuron under voltage-clamp (with C_m = 0.9 pF/cm^2, R_m = 20,000 Ωcm^2, and R_i = 150 ± 50 Ωcm). The idealized SC dendritic morphology has an uniform diameter of 0.47 µm and 3 dendritic branch points. Top traces, simulated qEPSCs (sim qEPSC) in response to a quantal synaptic conductance (g_{syn}) injected at the soma (magenta) and at a distance of 60 µm on a dendrite (grey traces). g_{syn} was set to reproduce the experimental quantal EPSCs following somatic synapses activation. Bottom traces (green), the corresponding local voltage transients at the site of synaptic conductance injection. Boundaries of shaded region indicate simulations with a R_i of 100 to 200 Ωcm. **(D)** 2PLSM image of a P16 SC (maximal intensity projection) patch- loaded with 30 µM Alexa 594 and the corresponding 3D reconstruction in *NeuronStudio* (red: soma, brown: dendrite, bleu: axon). **(E)** Superimposed numerical simulation of quantal EPSCs in the reconstructed P16 SC (with C_m = 0.9 pF/cm^2, R_m = 20,000 Ωcm^2, and R_i = 150 Ωcm) in response to an quantal conductance (g_{syn}) at the soma (red dot,

magenta trace) or at a distance of 60 μm on 6 different dendritic branches (blue dots, grey traces). g_{syn} is set to reproduce immature qEPSCs evoked by somatic synapses. **(F)** Sim qEPSC induced when synapses are activated at the soma (red dot, magenta trace) or on a single dendrite (blue dot, grey traces) Summary plot showing the sim qEPSC amplitude as a function of synaptic location along the somato-dendritic compartment. Boundaries of shaded region indicate simulations with a Ri of 100 to 200 Ωcm. (**G**) Same as in (D) but for a P42 SC. (**H**) same as in (F) but with the reconstructed P42 SC and g_{syn} to reproduce experimental adult somatic qEPSC.

Figure 3

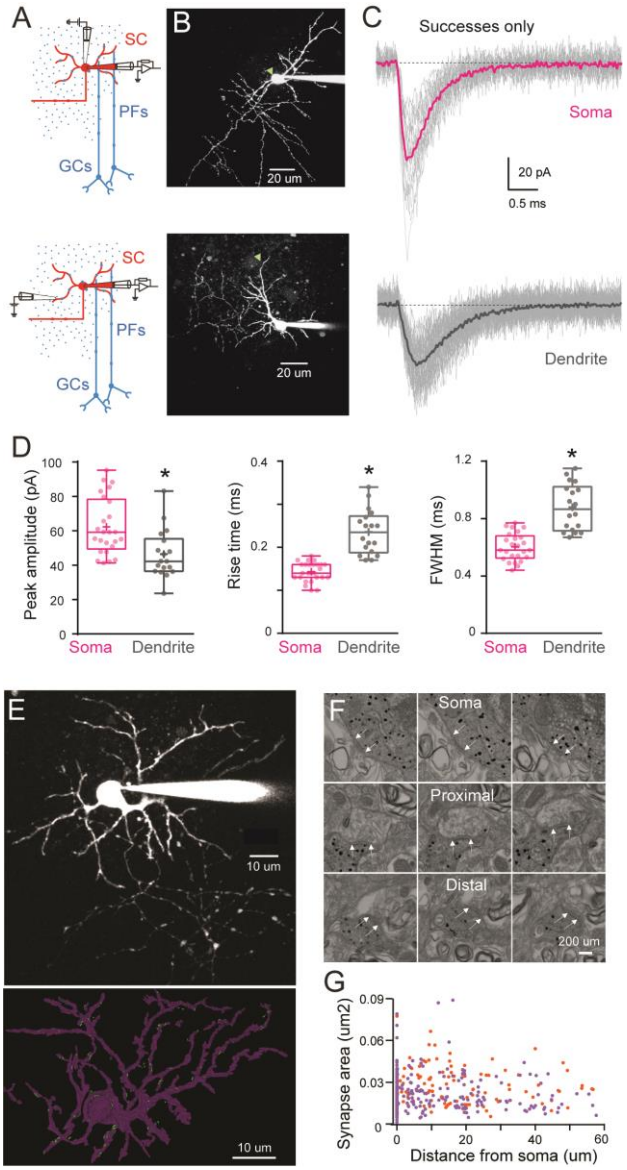

Figure 3. Difference in quantal EPSC properties and PSD area between the soma and dendrite in immature SC. (A) Diagram of a parasagittal cerebellar slice showing parallel fibers (PFs) projecting perpendicular (blue dots) to the dendritic plane of SCs (in red), allowing precise positioning of the stimulus electrode with respect to the soma (top panel) or an isolated SC dendrite (lower panel). **(B)** 2PLSM images (maximal intensity projection) of two immature SC loaded with the patch-pipette with 30 µM Alexa 594 with the location of stimulating pipette indicated with a green triangle. **(C)** Superimposed single qEPSCs (grey) from ***successful trials***, and the corresponding averaged traces (bold) recorded in response to extracellular stimulation at the soma (top) and on a dendrite (bottom) under low release probability conditions (external $[Ca^{2+}]/[Mg^{2+}]$ was 0.5/5 mM; failure rate >90%). **(D)** Box and whisker plots showing the median (line) peak amplitude, 10-90% rise time and full-width half maximum (half-width) following somatic (magenta) or dendritic (grey) synapses activation (n = 25 and n = 18 respectively), the 25th and 75th percentile (box), range (whiskers) and mean (+). Superimposed filled circle represent individual cells (asterisks denote $P<0.05$). **(E)** 2PLSM image of an Alexa 594 loaded P14 SC (maximal intensity projection) before fixation and(below) its 3D rendering after an EM reconstruction. Light dots indicate PSD locations. (**F**) Electron micrographs of an immunogold labeled SC soma with proximal and distal dendritic segments. The outer bound of excitatory synapses are indicated by arrows. Scale bar, 200nm (**G**) Plot of synapse area versus distance from soma. Orange and purple circles indicate data obtained from two immature SC (P14, n = 172 synapses and P17 n = 220 synapses - total n = 393).

Figure 4

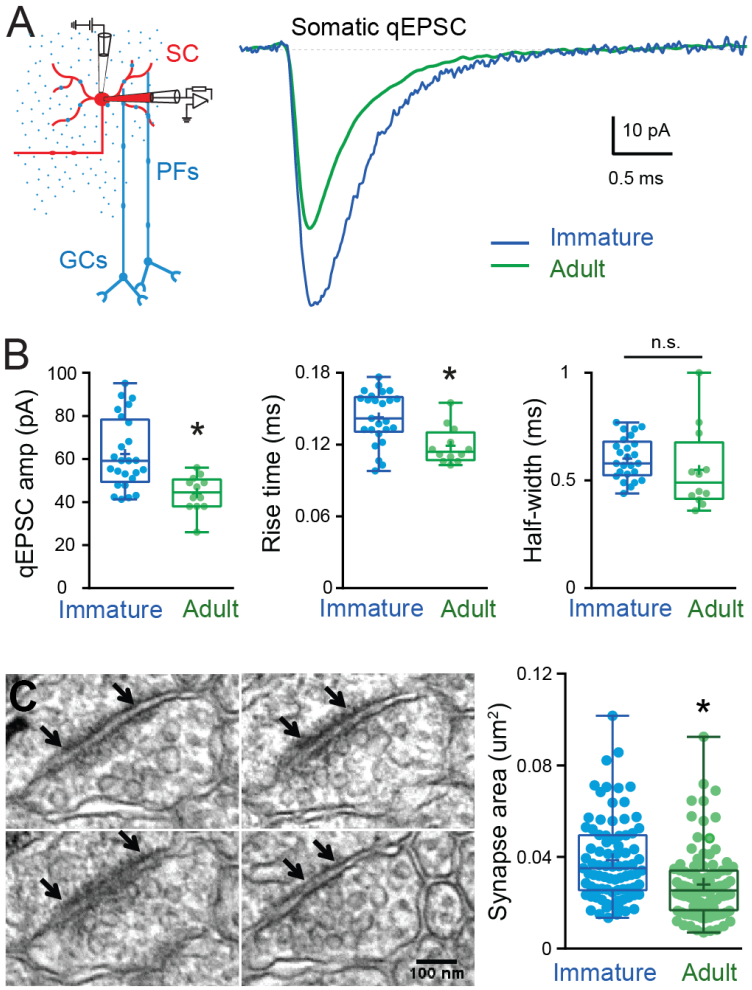

Figure 4. Developmental changes in somatic qEPSC properties and somatic PSD size. (A) Left panel shows a diagram of a parasagittal cerebellar slice showing parallel fibers (PFs) projecting perpendicular (blue dots) to the dendritic plane of a SC (in red), showing the stimulus electrode (top) position above the soma. Right panel shows superimposition of representative qEPSC averages aligned on event onset, from immature SC (blue trace) and adult SC (green trace, from Abrahamson *et al.*, 2012). **(B)** Summary box and whisker plot showing the qEPSC amplitude, 10-90% rise time and half-width for immature (blue, n = 25) and adult (green, n =12) SC (asterisks denote $P<0.05$). (**C**) Serial electron micrographs of an asymmetrical synapse made by axon terminals on an immature SC soma. Right panel : Summary box and whisker plot showing the synapse area obtained from immature (n =83 synapses from 3 cells) and adult SC (n = 97 synapses from 2 cells) somata. Superimposed filled circle represent individual synapses (asterisks denote $P<0.05$). The outer boundaries of an excitatory synapse are indicated by arrows. Scale bar, 100 nm.

1124 **Figure 5**

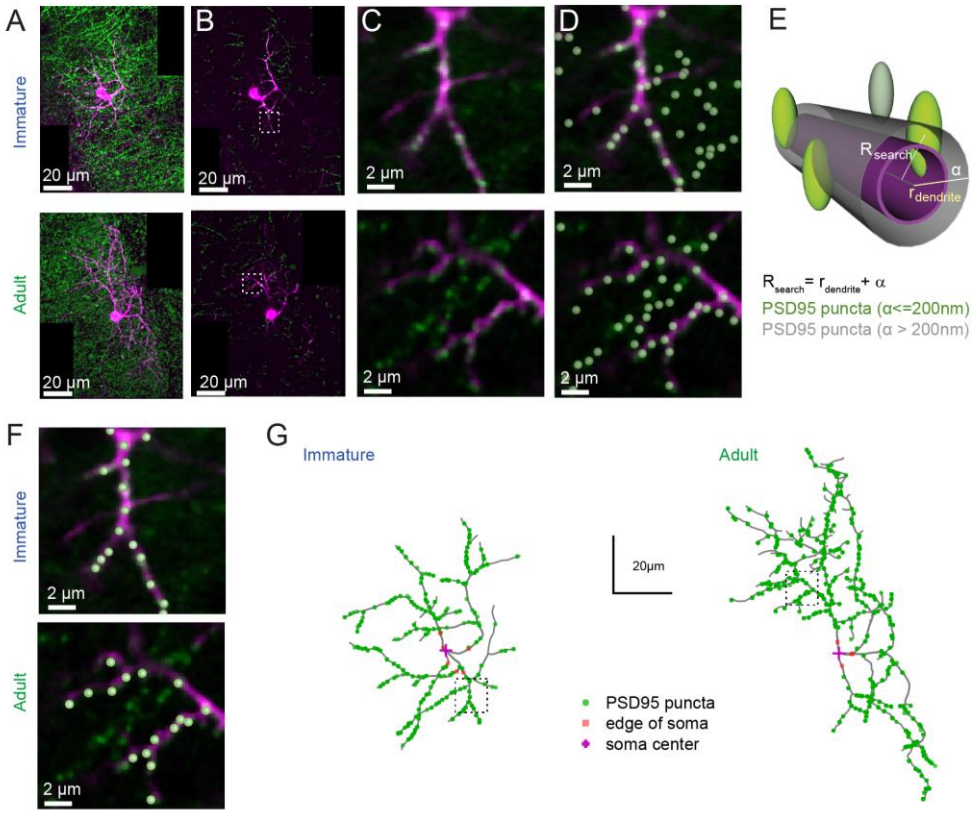

1125

1126 **Figure 5: PSD95 puncta distribution on immature and adult SC**. **(A)** Maximum intensity
1127 projection of merged images showing a P14 (top) and P42 (bottom) SC labelled with Alexa594
1128 (magenta) and venus-tagged PSD95 puncta (green). **(B)** Example of single optical sections from (A).
1129 **(C)** Inset indicated in (B) showing details of a dendritic branch with venus-tagged PSD95 puncta. **(D)**
1130 Detected PSD95 puncta on the same focal plane overlayed on the fluorescent image. (**E)** Diagram
1131 describing the criteria for asignement of PSD95 puncta to a dendrite branch. Puncta were considered
1132 as associated with the dendrite if their centers were located within a search radius (R_{search}) defined as
1133 the local dendritic radius $r_{dendrite}$ + α, where α = 0.2µm. (**F)** Examples of detected PSD95 puncta
1134 identified as connected to dendritic structure in an immature (top) and adult (bottom) SC. (**G)**
1135 Skeleton representation of the dendritic tree of an immature (left) and adult (right) SC with detected
1136 PSD95 puncta in green. The edge and the center of the soma are indicated by orange squares and
1137 magenta crosses, respectively.
1138
1139

Figure 6

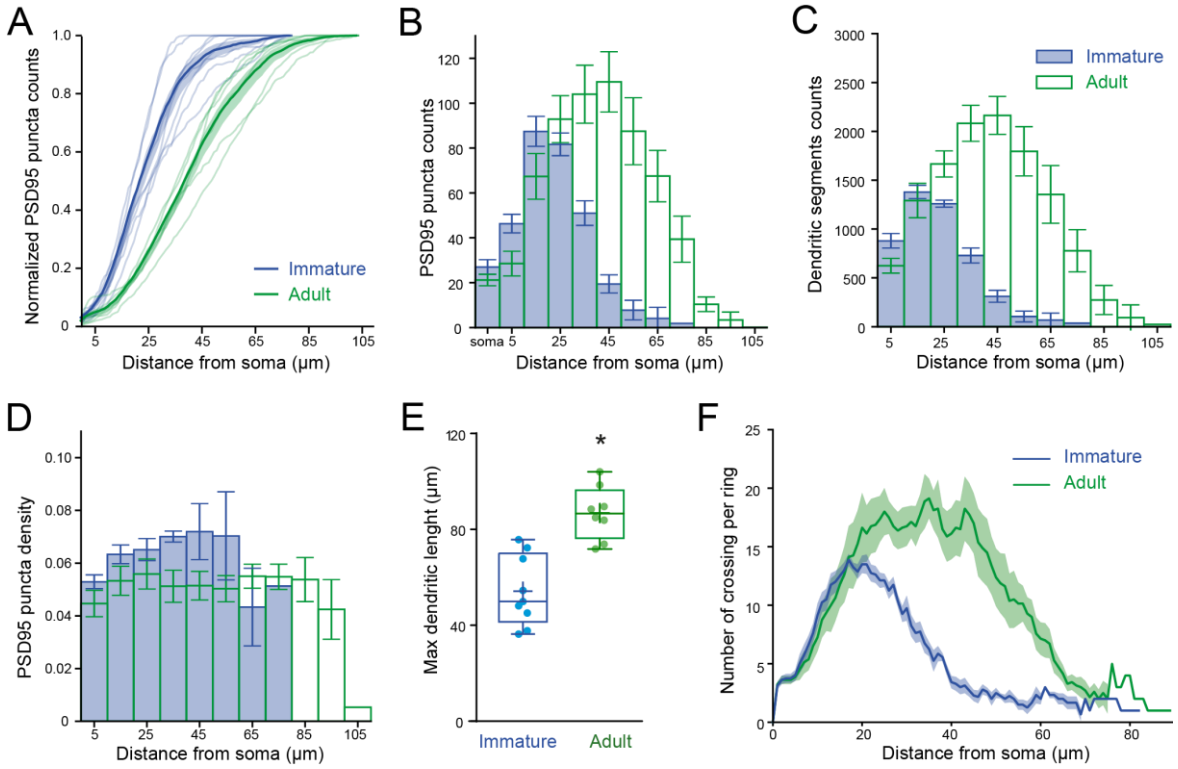

Figure 6: PSD95 puncta distribution and morphological analysis on immature and adult SC. (A) Cumulative plot showing venus-tagged PSD95 puncta distribution for individual and average (bold traces with boundaries of shaded region indicate SEM) obtained from 9 immature (blue) and 8 adult (green) SC (P<0.05, KS test). **(B)** Superimposed histograms of the mean PSD95 puncta count on the soma and dendrites of immature (blue) and adult (green) SC with a 10 µm increment. **(C)** Superimposed histograms of the average dendritic segment count (segment length of 100 nm) for immature (blue) and adult (green) SCs. **(D)** Dendritic mean PSD95 puncta density as a function of distance estimated from B and C (for all P>0.05 except at 35 µm; MW test). **(E)** Summary box and whisker plot showing the maximal dendritic length per neuron for immature and adult SC. Superimposed filled circle represent individual cells (asterisks denote P<0.05)**. (F)** Sholl analysis showing increased arbor complexity with development.

Figure 7

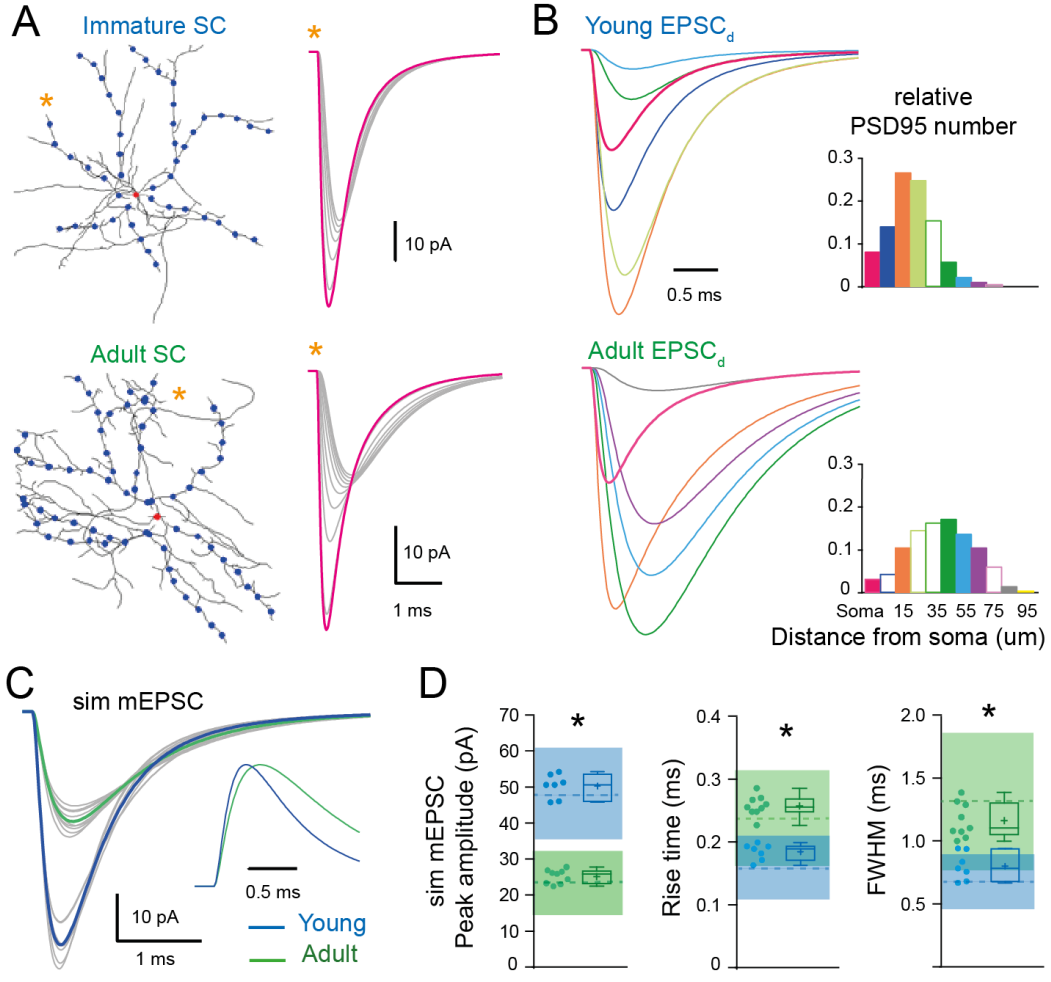

Figure 7. The developmental change in synaptic distribution recapitulates the developmental change in mEPSC properties (A) Numerical simulations of somatic and dendritic qEPSCs for synapses placed on the soma (red dot) and at 10 µm intervals (blue dots) along 7 of the longest dendrites of a reconstructed immature (P16; top) and 9 of the longest dendrites of a reconstructed adult (P42; bottom) SC (with C_m = 0.9 pF/cm^2, R_m = 20,000 Ωcm^2, R_i = 150 ± 50 Ωcm). Right panel shows example of qEPSC for somatic (magenta) and dendritic (grey traces) synapses along a single dendrite labeled with an asterisk. The synaptic quantal conductances g_{syn} were set to reproduce the experimental qEPSCs when stimulating somatic synapses at both ages. **(B)** The relative frequency of the excitatory synapse distribution (right panel) was used to scale each qEPSC to produce a normalized qEPSC$_d$ describing its relative contribution of the mean mEPSC waveform. **(C)** Superimposed mEPSC waveform obtained from added the qEPSC$_d$ for each dendrites (grey) and the corresponding average mEPSC (bold) obtained from the immature SC (P17, blue trace) and adult SC (P44, green trace). Inset: traces normalized to their peak. **(D)** Summary box and whisker plots showing the median (line) peak amplitude, 10-90% rise time and decay, the 25th and 75th percentile (box), range (whiskers) and mean (+) of the sim mEPSC for the immature (blue) and adult (green) SCs. Individual dendritic mEPSCs are illustrated with filled circles (asterisks denote P<0.05). Dotted line shows the experimental mEPSC average values ± 1 SD (shaded region).

Figure 8

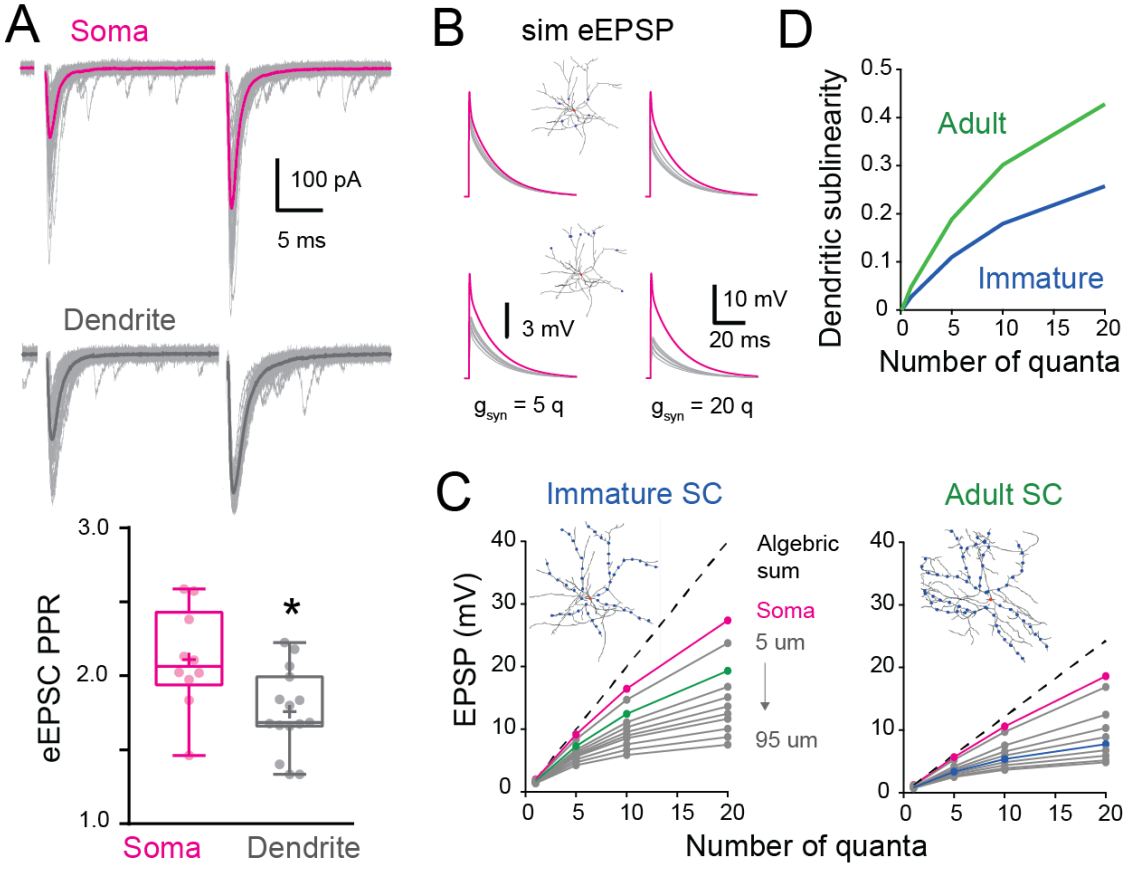

Figure 8 : Location dependence of short-term plasticity and sublinear behavior in immature SC **(A)** Superimposed recorded single evoked EPSCs (grey) and the corresponding average (bold) in response to a pair of extracellular stimuli (50hz) when the stimulation electrode is placed above the soma (magenta) and distally on an isolated dendrite (grey). Bottom: summary box and whisker plot of paired-pulse ratio of EPSC amplitudes (PPR = $EPSC_2/EPSC_1$) for somatic synapses (n = 10) and dendritic synapses (n = 15). The PPR ratio was assessed from recordings where the first EPSC had an amplitude inferior to 400 pA and had a failure rate below 30% (for somatic synapses, Amp = 239.4 ± 32 pA with a half-width = 0.88 ± 0.07 ms, n = 10). Superimposed filled circles represent individual cells (asterisks denote $P<0.05$). **(B)** Simulated evoked EPSP (sim eEPSP) under current-clamp conditions for synapses at the soma (magenta) and at 20 or 60 µm on dendrites (grey) of a reconstructed immature SC. g_{syn} peak amplitude is set at 5 or 20 quanta *ie* is a multiple of the g_{syn} that produce a qEPSC for somatic synapses. **(C)** Subthreshold input-output relationship of sim eEPSPs obtained by plotting the average peak sim eEPSP amplitude for an increase number of quanta as the function the algebraic sum of the sim eEPSP of a reconstructed immature (left) and adult (right) SC. The dotted black line has a slope of 1. The circles indicate sim eEPSP resulting from a g_{syn} peak amplitude of 1, 5, 10 and 20 quanta. **(D)** Summary plot showing dendritic sublinearity (1- (dendritic EPSP amp/soma EPSP amp) with EPSP converted to number of quanta) as a function of number of quanta for reconstructed immature (blue) and adult (green) SCs.